

Revealing the Photochemical Pathways of Nitrate in Water through First-Principles Simulations

Kam-Tung Chan,[†] Margaret L. Berrens,[†] Zekun Chen,[†] C. William McCurdy,[†]
Cort Anastasio,[‡] and Davide Donadio^{*,†}

[†]*Department of Chemistry, University of California, Davis, One Shields Ave., Davis, CA
95616 USA*

[‡]*Department of Land, Air, and Water Resources, University of California Davis, One
Shields Ave. Davis, CA, 95616.*

E-mail: ddonadio@ucdavis.edu

Abstract

Nitrate anion (NO_3^-) is a ubiquitous species in aqueous phases in the environment, including atmospheric particles, aerosol droplets, surface waters, and snow. The photolysis of NO_3^- is a 'renoxification' process, which converts NO_3^- solvated in water or deposited on surfaces back into NOx to the atmosphere. NO_3^- photolysis under environmental conditions can follow two channels: (1) NO_2 and O^- ; (2) NO_2^- and O (${}^3\text{P}$). Despite the well-studied macroscopic kinetics of the two channels, the microscopic picture of the photolysis still needs to be explored. Furthermore, previous experiments have shown that NO_3^- photolysis in aqueous solutions has a low quantum yield of ~1%, leading to a solvation cage effect hypothesis. A previous theoretical study has indicated that the low quantum yield may be due to the direct spin-forbidden absorption of NO_3^- to its triplet state. Here, we employ first-principles molecular dynamics

simulations at the level of hybrid DFT with enhanced sampling to explore the two channels in an aqueous solution to unravel the atomistic and electronic structure details of the photolysis, as well as investigate the causes of its low quantum yield under a solvation environment. The direct spin-forbidden absorption to T_1 state is viable through spin-orbit coupling and is ~ 15 times weaker than the spin-allowed absorption to S_1 state. A solvation cage complex is identified as a metastable state that requires additional thermal energy to complete the dissociation of the N-O bond at the triplet state. This metastable state allows the photo fragments to recombine or deactivate through non-radiative processes. Our simulations also qualitatively explain the temperature dependence of the two channels observed in experiments based on the rearrangement of H-bonds. This work provides a novel molecular picture illustrating the significantly low quantum yield and temperature dependence of NO_3^- photolysis under environmental conditions and a starting point for future studies of environmental nitrate photochemistry.

Introduction

The nitrate anion (NO_3^-) is a primary species in the global nitrogen cycle.¹ It is ubiquitous in the environment, including aerosol particles, surface waters, and Polar snow. Atmospheric NO_3^- is formed from the oxidation of NOx ($\text{NO} + \text{NO}_2$), which is emitted by fossil fuel combustion and other sources.^{2,3} Under environmental conditions, NO_3^- in solution absorbs light over a broad band centered at ~ 300 nm, i.e., 4.1 eV, and photolysis can occur via two channels:^{4,5}



NO_3^- photolysis is a 'renoxification' process, which plays an essential role in the formation of secondary atmospheric aerosols and oxidants.^{3,6} Recent field observations in the marine

atmosphere indicate that NO_3^- photolysis in sea salt aerosols is a significant source of NOx,^{7–9} accounting for the missing source of NOx in a macroscopic chemical model of the atmosphere over the oceans.¹⁰ Furthermore, NO_3^- photolysis can play a crucial role in sulfate formation during the co-uptake of SO_2 and NO_2 by sea salt aerosols.¹¹ Therefore, the photolysis of NO_3^- under environmental conditions is of great interest to the environmental science community.

Secondary products of NO_3^- photolysis have an environmental impact too. In the presence of water molecules, the O^- produced in Channel (1) is rapidly protonated to form a hydroxyl radical, which is one of the most important oxidants in the atmosphere.^{1,2} Under acidic conditions, NO_2^- generated in Channel (2) is converted to its protonated form nitrous acid (HONO), which is also a crucial photochemical source of hydroxyl radical and nitric oxide.¹²

NO_3^- photolysis in solution has been studied for decades.^{4,12–17} Experiments show that in an aqueous solution at room temperature, the quantum yields of the two channels are comparable, with $1.2 \pm 0.2\%$ for Channel (1) and $1.1 \pm 0.2\%$ for Channel (2).^{12,15} Such very low quantum yields led to the hypothesis of a solvation cage effect, in which the dissociated fragments recombine before they diffuse out of a cage of hydrogen-bonded water molecules.^{18–21} This hypothesis is supported by experiments showing the enhancement of NO_3^- photolysis rates at the air-water and air-ice interfaces, where the solvation cage effect may be weakened.^{22–27} *Ab initio* molecular dynamics (AIMD) simulations probing the structure of the solvation shell of ground-state NO_3^- in water and at the air-ice interface are not conclusive in this regard, and calculations of the UV-visible absorption spectrum exclude that photolysis rate enhancement could be even partially attributed to a solvatochromic shift, in contrast to the case of organic pollutants.^{28–30}

The relative significance of the two channels at different conditions is also still unclear. Experiments suggest that Channel (1) is more favorable at higher temperatures, whereas Channel (2) is more prominent at lower temperatures, especially in the liquid-like pockets in ice.³¹ Scharko et al. observed that Channel (2) has a higher yield in acidic aqueous solutions as it produces HONO.¹⁷ This secondary reaction was also predicted by AIMD simulations

in the ground state.³² Besides the acidity, Scharko et al. suggested that the hydrolysis of NO₂ generated in Channel (1) can also be responsible for additional HONO formation, in aqueous solutions.¹⁷ Hullar et al. observed that the quantum yield of NO₂⁻ in a quasi-liquid layer at the air-ice interface is enhanced by a factor of 6.4 over a bulk aqueous solution at the same temperature.²⁷ Considering these experimental findings, factors other than secondary reactions should be responsible for the enhancement of the quantum yield at the air-ice interface.

Quantum chemical calculations of the excited state NO₃⁻ revealed that only Channel (2) is energetically viable in the gas phase and in implicit solvent models.³³⁻³⁷ The lowest energy spin-allowed excitation for NO₃⁻ corresponds to a S₀ → S₁ symmetry forbidden n → π* transition that can be enabled only by coupling with vibrational modes.^{33,34,36} The S₁ state may be unbound as its gas-phase energy is close to the electron detachment energy, and we are not aware of any experimental gas-phase observations of bound excited states of NO₃⁻.^{34-36,38,39} In solution, the electron affinity increases, and the symmetry of NO₃⁻ is lowered from D_{3h} to C_{2v} favoring light absorption and photolysis under environmental conditions.^{25,36} However, the S₁ potential energy surface is not conducive to Channel (2), as the products are in the triplet state. As intersystem crossing from the S₁ state is unlikely, Svoboda and Slavíček suggested that NO₃⁻ photolysis may be enabled by direct spin-forbidden absorption from S₀ to the first triplet state T₁.³⁵ Furthermore, a minimum energy conical intersection between the S₀ and S₁ states near the FC point suggests that the majority of S₁ excited NO₃⁻ undergoes a non-radiative deactivation to the ground state. These results call for further investigation of NO₃⁻ photolysis in an explicit solvation environment to assess the hypothesis of direct spin-forbidden absorption and probe the molecular mechanisms that enable Channel (1).

Here, we explore NO₃⁻ photolysis in water by AIMD in the first excited triplet state, explicitly modeling the solvation environment and exploring the reaction free energy surface with enhanced sampling. We first calculate the potential energy surfaces of the low-lying

singlet and triplet states of NO_3^- along the dissociation coordinate in the gas phase with multi-reference quantum chemical methods to assess the dissociation limit of each electronic state and to assess the accuracy of a hybrid density functional for this problem. We then sample the ground state configurations (S_0) of NO_3^- in water at room temperature by AIMD and compute the UV-visible absorption spectrum by time-dependent density functional theory (TDDFT), including both the spin-allowed and the direct spin-forbidden excitations,⁴⁰ exploiting a multimodel approach established in previous works.^{28,41} We find that the direct spin-forbidden absorption to the T_1 state is viable through spin-orbit coupling, although about 15 times weaker than the spin-allowed absorption to the S_1 state. We follow by using *ab initio* metadynamics^{42–44} to simulate the dissociation of NO_3^- in the explicit water in the T_1 state, from which we obtain free energy barriers and reaction rates to compute the quantum yield of the two reaction channels with a master equation model. These simulations show that surrounding water molecules trap NO_3^- (T_1) in a weakly metastable solvation cage complex. From the solvation cage complex, the system may evolve through either Channel (1) or (2) with a relative likelihood dictated by the different rearrangement of the hydrogen bonding in the solvation shell of the products, thus explaining the temperature dependence observed in experiments. The current study provides a novel microscopic picture illustrating the low experimental quantum yields of NO_3^- photolysis in aqueous solvation environments.

Computational Methods

Quantum Chemical Calculations

Before performing AIMD simulations of solvated nitrate, we computed the potential energy surface of gas phase NO_3^- along the N-O dissociation coordinate in the ground state and the low-lying triplet and singlet excited states at the level of multi-reference N-electron valence state perturbation theory at the second order with the quasi-degenerate extension (QD-NEVPT2) to account for correlation.^{45,46} The ground state geometries along the N-O

bond dissociation coordinate were first optimized at the level of broken-symmetry DFT with CAM-B3LYP range-separated hybrid density functional and ma-def2-TZVP basis set.^{47–49} It has been found that the equilibrium structure computed by the CAM-B3LYP functional and a triple-zeta basis set agrees well with CCSD values.³⁶ The QD-NEVPT2 calculations were then performed over the optimized ground state geometries to build up the potential energy surfaces of the low-lying singlet and triplet excited states. The orbitals and references used in the QD-NEVPT2 calculations were obtained by previous state-averaged complete active space self-consistent field (SA-CASSCF) calculations.⁵⁰ For each geometry along the dissociation coordinate, the SA-CASSCF calculations considered an active space of ten electrons in nine orbitals. Three singlet states (including the ground state) and four triplet states were included in the calculations. The strongly contracted formalism of NEVPT2 was used with the quasi-degenerate extension based on Van Vleck perturbation theory using the aug-cc-pVTZ basis set.^{51–53} The vertical excitation energies from the equilibrium geometry were compared with the multi-reference configuration interaction method with Davidson correction for linked quadruples (MRCI+Q) using the same active space and basis set.⁵⁴ To assess the reliability of the DFT framework that we use to simulate the reaction in with explicit water, we also performed the same calculations on the ground state and the T₁ state using the hybrid functional revPBE0^{55,56} with D3 dispersion correction⁵⁷ and the def2-SVP basis set^{58,59} (see section S1). The solvation model of density (SMD)⁶⁰ was used to account for the implicit solvation in water. This hybrid functional with dispersion correction was later used for simulating the dissociation dynamics at the T₁ state with explicit waters. All the potential energy surface calculations in the gas phase and under implicit solvation were carried out with ORCA 5.0.2.⁶¹

Ab Initio Molecular Dynamics Simulations

To capture the local effect of hydrogen bonding on the light absorption and photodissociation of NO₃⁻, we performed AIMD simulations of a bulk ammonium nitrate aqueous solution with

explicit water. DFT-based AIMD simulations were performed using Quickstep⁶² in the CP2K 8.2 package.⁶³ The nuclear dynamics were propagated by the Born-Oppenheimer forces. A convergence criterion of 1×10^{-5} Hartree was used to optimize the wave function. The hybrid exchange-correlation density functional revPBE0 with Grimme dispersion correction (D3) was employed to evolve the dynamics of a 12.98 x 12.98 x 12.98 Å box with 1 unit of NH₄NO₃ and 63 water molecules with periodic boundary condition for an aqueous solution model.^{55–57} Previous studies have shown that revPBE0-D3 provides a good description of water and aqueous systems.^{64,65} The ammonium ion was used as a counterion because it is abundant in atmospheric droplets and particulates containing NO₃⁻.² Valence Kohn-Sham orbitals were expanded in the DZVP Gaussian basis set together with the plane-waves auxiliary basis set, while core states were treated implicitly using Goedecker–Teter–Hutter pseudopotentials.^{66–68} A 400 Ry energy cutoff was set for the plane-wave basis set. AIMD simulations in an aqueous solution were run under the canonical (NVT) ensemble with a temperature of 300 K using the stochastic velocity-rescaling thermostat with a 100 ps coupling time.⁶⁹ In these simulations, hydrogen atoms were replaced with deuterium, thus allowing a relatively large timestep of 0.5 fs to integrate the equations of motion. The system was run for 25 ps in total, with the first 5 ps serving as the equilibration and 20 ps serving as the production run.

Former studies have shown that NO₃⁻ in aqueous solutions, adsorption, and solvation at the air-water and air-ice interfaces are accurately reproduced using a semi-local density functional with dispersion corrections.^{28,70–72} However, to model the S₀ → T₁ transition, semi-local density functionals should not be used, as they lead to a substantial underestimate of the energy gap of solvent in which NO₃⁻ is embedded. In particular, for the case of water, the energy difference between the valence and the conduction band with the Perdew, Burke, Ernzerhof (PBE) functional⁷³ is only 4 eV, as opposed to ~9 eV as expected from experiments and higher-level electronic structure calculations.^{74–77} Recalling that the vertical excitation energy of NO₃⁻ is ~4 eV, triplet state NO₃⁻ at the PBE level is quasi-degenerate with

the water conduction band. This causes an unphysical electron delocalization and drives dissociation along Channel (1), which turns out to be the only possible pathway (see section S2 and Figure S2 for details). In this respect, a hybrid density functional with dispersion corrections, revPBE0-D3, was used as it provides a more realistic representation of the electronic structure of materials despite an increased computational cost.^{55–57,78,79}

UV-Visible Absorption Spectra Calculations

To compute the finite temperature UV-visible absorption spectrum of solvated NO_3^- , we adopted a multimodel approach that proved accurate and predictive for organic solvents and ammonium nitrate.^{28,29,41} The oscillator strengths and UV-visible absorption energies were calculated as the ensemble average of 800 vertical excitations from the individual frames extracted from the 20 ps production run. These extracted frames were embedded in a hybrid solvation model, where the first two solvation shells of NO_3^- , which corresponded to 12 water molecules, were treated explicitly, and the long-range screening was accounted by the CPCM polarizable implicit solvent, with a static dielectric constant of 80.3 and refractive index 1.33.⁸⁰ The oscillator strengths of $S_0 \rightarrow S_1$ and $S_0 \rightarrow T_1$ transitions, as well as the UV-visible absorption spectra at a finite temperature were calculated at the level of TDDFT, with CAM-B3LYP functional.⁴⁸ It has been shown that CAM-B3LYP accurately models the excited states of NO_3^- under implicit solvation and solvated by a small water cluster.^{34–36} The spin-forbidden absorption was calculated by including spin-orbit coupling between singlet and triplet states using quasi-degenerate perturbation theory.⁸¹ All the TDDFT calculations were performed using a ma-def2-TZVP basis set⁴⁹ along with the resolution of identity approximation for the Coulomb and exchange integrals using the ORCA 5.0.2 package.⁶¹ The UV-visible spectra were obtained from the Gaussian envelopes with an empirical broadening width of 0.027 eV.

Ab Initio Metadynamics in the T₁ State

Under the assumption of a direct spin-forbidden transition to the T₁ State, the system was simulated in the T₁ state at the level of spin-polarized hybrid DFT (revPBE0-D3), to probe the dissociation dynamics of NO₃⁻. The computational details of all AIMD simulations at the T₁ were the same as the AIMD simulations in the ground state.

Preliminary simulations show that NO₃⁻ (T₁) is metastable and does not dissociate spontaneously within 2 ps, as opposed to the spontaneous dissociation in gas-phase photochemistry (see Figure S3). Well-tempered metadynamics^{43,44} was used as an enhanced sampling method to overcome and estimate the dissociation barrier and explore the reaction free energy landscape. In metadynamics simulations, a bias potential is continuously applied to the system, which depends on the set of predefined collective variables (CVs), where CVs are functions of atomic positions.⁴⁴ In this study, well-tempered metadynamics was used in which the height of the deposited Gaussians would decrease exponentially as the bias is applied:

$$V_n(s) = \sum_{k=1}^n G(s, s_k) e^{-\frac{\beta}{\gamma-1} V_{k-1}(s_k)} \quad (3)$$

where $G(s, s_k) = W e^{-\frac{(s-s_k)^2}{2\sigma^2}}$ is a Gaussian centered in the CV value s_k at time t_k , $\beta = \frac{1}{k_B T}$, γ is the bias factor, and σ is the width of the Gaussian.

Two CVs (d, n) were chosen to be applied to the well-tempered metadynamics simulation (Figure 1). The first CV, d , is the distance between atom N and O1, corresponding to the dissociation coordinate. However, it is not enough to differentiate the two dissociation channels. Since the two channels only differ in the net negative charge localization and are comparable in an aqueous solution, one can hypothesize that the solvation structure of NO₃⁻ is crucial to determine which channel it will eventually proceed. Based on this hypothesis, a second CV, n , was used to describe the number of H atoms surrounding atoms O2 and O3 (see Figure 1). While the net negative charge of NO₂⁻ makes it form hydrogen bonds with water, it has been shown that NO₂ does not form extensive hydrogen bonds with water.⁸²

Therefore, the number of H atoms surrounding atoms O₂ and O₃ can be a suitable CV candidate to drive the dissociation and differentiate the two channels. This number, n , is defined as follow:

$$n = \sum_{i \in O_2, O_3} \sum_{j \in H_w} s_{ij} \quad (4)$$

where H_w refers to the H atoms of water, s_{ij} is a switching function and is defined as

$$s_{ij} = \frac{1}{2} \left[\frac{1 - (\frac{r_{ij}}{r_0})^n}{1 - (\frac{r_{ij}}{r_0})^m} \right] \quad (5)$$

where r_{ij} is the distance between atoms i and j . r_0 is set to be 2.55 Å, and n and m are set to 8 and 16, respectively. The parameters were determined by fitting the switching function s_{ij} with the radial distribution function of the O_n–H_w pair obtained from the equilibrium simulation, where O_n refers to the O atoms of NO₃⁻.

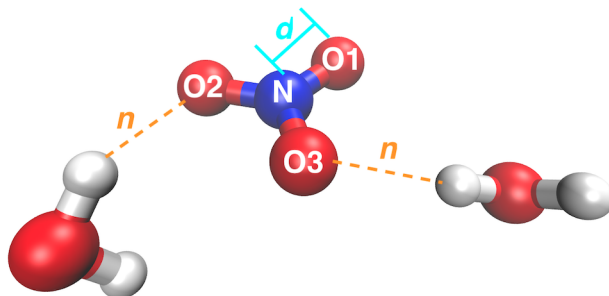


Figure 1: Schematic representation of the CVs used in the current study. The two CVs, d are colored in cyan and orange respectively

The well-tempered metadynamics simulation was carried out at the T₁ state after a 2 ps unbiased equilibration run initiated by exciting a ground-state configuration in the T₁ state. The initial height of the Gaussian W was 5.0 kJ/mol, and the widths were 0.1 Å and 0.15. The bias factor was set at 25. A new Gaussian was deposited at every 25 fs. A harmonic restraining potential wall with a force constant of 100 kJ/mol Å² was applied on d when it was greater than 4 Å to limit the exploration of the dissociated state. To better exploit parallel hardware architecture and enhance the sampling efficiency, we employed

the multiple walkers approach.⁸³ In a multiple walkers metadynamics simulation, multiple simulations (walkers) explore the same free energy surface (FES), contributing to the same history-dependent bias potential. Two walkers were used in the current study, and the update frequency of the sharing between the two deposited biases was set to 0.5 ps. The multiple-walkers well-tempered metadynamics simulations were run for 52 ps (26 ps for each walker). The FES was calculated by reweighing the frames from the two walkers using the time dependence of the metadynamics bias potential. The convergence was evaluated by the diffusion of CVs (recrossings of the free energy barriers) and the average error of the relative free energy against time through block analysis.^{84,85}

We calculated the rate constants from the free energy barriers using transition state theory. For the non-radiative deactivation to the ground state through intersystem crossing, we applied Fermi's golden rule combined with the path integral approach.^{86–88} This method includes the coupling of electronic spin-orbit coupling with vibrational degrees of freedom, which can describe the intersystem crossing rates of small organic molecules with negligible electronic spin-orbit coupling.⁸⁹ A recent study showed that this method can estimate the intersystem crossing rates of small aromatic organic molecules qualitatively.⁹⁰ More details on these calculations are provided in section S6.

Results and Discussion

Potential Energy Surfaces in the Gas Phase

In solution, NO_3^- absorbs light over a broad band with a maximum at 305 nm corresponding to 4.05 eV. Gas-phase calculations indicate that this energy corresponds to the $S_0 \rightarrow S_1$ transition. S_1 and T_1 states are the only relevant excited states under environmental conditions as the energy absorption band is at the high energy edge of the solar spectrum. We computed the main features of the gas-phase photodissociation potential energy surface by *ab initio* quantum chemical methods and DFT using the same functional as in the AIMD

Table 1: Gas-phase excitation, electron detachment, and dissociation energies relative to the NO_3^- (S_0) ground state in eV computed with different quantum chemical methods and with density functional theory.

Species	NEVPT2(10,9) /aug-cc-pVTZ	MRCI(10,9) /aug-cc-pVTZ	EOM-CCSD /aug-cc-pVQZ ^a	revPBE0 /aug-cc-pVTZ	Experiment ^b
NO_3^- (S_1)	4.42	3.81	4.08	4.07*	-
NO_3^- (T_1)	4.18	3.63	3.88	3.67*	-
NO_3^\cdot	4.38	3.90		3.91	3.92
$\text{NO}_2 + \text{O}^-$	5.21	4.10	-	4.53	-
$\text{NO}_2^- + \text{O}$ (${}^3\text{P}$)	4.01	3.40	-	3.87	-

^a Ref.³⁵

^b Ref.³⁹

* Calculated at the level of TDDFT.

simulations. The vertical excitation energies, the energies of the photolysis products, and the vertical electron detachment energy, calculated by QD-NEVPT2, MRCI+Q, and DFT, are reported in Table 1. The excitation energies to the T_1 and S_1 states are very close to the vertical electron detachment energy which was formerly measured as ~ 3.9 eV.^{38,39} In fact, bound excited states of negatively charged complex anions were never observed experimentally. Both MRCI and DFT calculations reproduce the experimental vertical electron detachment energy whereas QD-NEVPT2 overestimates it (4.38 eV). All three methods suggest that the T_1 state should be bound in the gas phase (Table 1 and S1). We speculate here that the T_1 state might be bound in the gas phase, although these calculations cannot firmly establish its existence. In contrast, both QD-NEVPT2 and MRCI+Q predict the S_1 excitation energy to be within 0.1 eV of the electron detachment energy, with QD-NEVPT2 slightly higher and MRCI+Q lower. These results are in agreement with previous EOM-CCSD calculations³⁵ and suggest that the S_1 state of NO_3^- is not bound in gas phase. However, experiments show that the electron detachment energy increases from ~ 3.9 eV to ~ 6.1 eV under aqueous solvation.³⁹ In contrast, the excitation energy to the S_1 state does not shift upon solvation and remains ~ 4.1 eV.^{39,91,92} Therefore, the S_1 state of NO_3^- becomes a bound state in solution.

Although electron detachment and excitation energies at the QD-NEVPT2 level are sys-

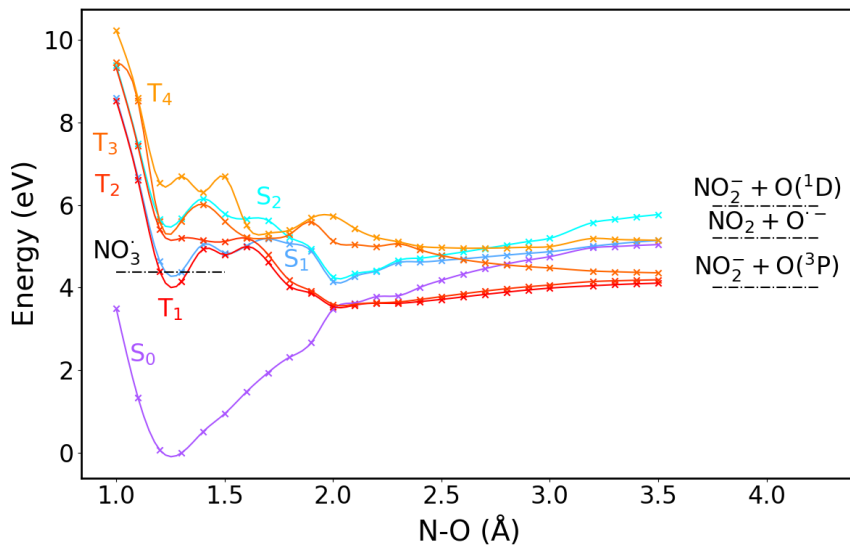


Figure 2: Potential energy curves of the low-lying electronic states of gas-phase NO_3^- calculated at the QD-NEVPT2(10,9)/aug-cc-pVTZ level. The total energies of the isolated species after dissociation are shown in dashed lines.

tematically overestimated compared with MRCI+Q and experiments, the former more computationally efficient method provides the same energy difference of ~ 0.2 eV between the S_1 and T_1 states, in agreement with Ref.³⁵ Hence we use QD-NEVPT2 to calculate the potential energy surfaces of the low-lying electronic states of gas-phase NO_3^- along the dissociation coordinate (Figure 2). The dissociation limit of the S_0 state corresponds to Channel (1). While the dissociation limit of the S_1 state is the same as the S_0 state, the S_2 state produces a NO_2^- and an O atom at its lowest singlet excited state (^1D). The three lowest triplet states (T_1 , T_2 , and T_3) dissociate into Channel (2). Conversely, T_4 dissociates into Channel (1), and it is degenerate with the dissociation limits of the S_0 and S_1 states. This calculation verifies the suggestion that singlet and triplet states are degenerate at the dissociation limit of Channel (1). It is worth noting that the S_1 and T_1 states are quasi-degenerate for intact NO_3^- . This also matches the previously calculated potential energy surfaces of the two states at MRCI level.³⁵

To further assess the reliability of the hybrid functional with dispersion correction, which was used to simulate the dissociation dynamics at the T_1 state in an aqueous solution, we

scanned the ground state and the T₁ potential energy surfaces at the level of revPBE0-D3/def-SVP with an implicit solvation model (see Figure S1). The potential energy curves of the two states agree qualitatively with the NEVPT2 calculations in Figure 2. These results and the energies reported in Table 1 show that revPBE0-D3 with a double zeta basis set is reliable in providing the correct dissociation limits in aqueous solution.

Gas phase calculations support the former observation that only Channel (2) is energetically viable, as the products of Channel (1) are about 1 eV higher in energy (see Table 1).³⁵ To make Channel (1) viable, its relative energy should be lowered when NO₃⁻ is solvated in water. In fact, Svoboda and Slavíček calculated the reaction Gibbs free energies for both channels from the reaction Gibbs free energies in the gas phase and the hydration Gibbs free energies for all species. They have found that the energy difference of Channel (1) is indeed lowered and becomes energetically plausible under implicit aqueous solvation at a finite temperature.³⁵ This suggests that NO₃⁻ photolysis under aqueous solvation can proceed to both channels on the triplet potential energy surface. We notice that the S₁ and T₁ potential energy curves Figure 2 exhibit a significant dissociation barrier. This may be due to the system not being adiabatically optimized on the excited state surfaces, as the excited state energies were calculated from optimized ground state structures.

Direct S₀ → T₁ Excitation in an Aqueous Solution

Even though the direct S₀ → T₁ transition is spin-forbidden, it may be enabled by spin-orbit coupling, and can be computed using quasi-degenerate perturbation theory.⁸¹ Here, we assess the significance of the direct spin-forbidden transition of NO₃⁻ in an aqueous solution at room temperature by calculating the oscillator strengths and the UV-visible absorption spectra at the level of TDDFT. We use a mixed implicit/explicit solvent approach, treating explicitly the water molecules in the first and second solvation shells of NO₃⁻ (see also²⁸). Table 2 summarizes the calculated excitation energies and oscillator strengths compared with experimental values.^{91,92} The calculated excitation energy of the S₁ state agrees with

the light absorption measurements remarkably well. Due to the limited available statistics, the calculated oscillator strength of the S_1 excitation has a large uncertainty. However, it has an order of magnitude ranging from 10^{-5} to 10^{-4} , which agrees with the experimental values in the literature.^{91,92} This range of values is low, as the $S_0 \rightarrow S_1$ transition is symmetry forbidden and it is enabled only by the finite temperature dynamics of NO_3^- and symmetry breaking effect of the solvation environment.

Spin-orbit coupling calculations allow us to determine the excitation energy of the $S_0 \rightarrow T_1$ transition as 3.74 eV (~ 330 nm) with an oscillator strength of 4×10^{-6} . Comparing the oscillator strengths between the two absorptions indicates that the direct spin-forbidden transition is about 15 times weaker than the spin-allowed transition.

Table 2: Excitation energies and oscillator strengths of the S_1 and T_1 transitions in aqueous solution with 95% confidence intervals.

Method	ΔE_{S_1} (eV)	ΔE_{T_1} (eV)	f_{S_1}	f_{T_1}
CAM-B3LYP /def2-TZVP+ CPCM	4.13 ± 0.01	3.74 ± 0.01	$(7.50 \pm 0.45) \times 10^{-5}$	$(4.33 \pm 0.02) \times 10^{-6}$
Experiment	4.11 [†]		7×10^{-5} [†]	
	4.13 [‡]		2.5×10^{-4} [‡]	

[†] Ref.⁹¹

[‡] Ref.⁹²

Figure 3 shows that the direct excitation to T_1 can contribute to the low-energy tail of the UV-visible absorption band observed in experiments. The experimental UV-visible absorption spectrum shows a broad peak from 280 to 340 nm and is centered at 302 nm, which is usually assigned as the absorption corresponding to the S_1 state (see Figure 3). The calculated spectrum of the S_1 excitation agrees well with the experimental spectrum in terms of λ_{max} but is substantially narrower. Experimentally, the absorption peak corresponding to the T_1 state may be buried in this broad absorption peak due to its low oscillator strength. Our calculations confirm this hypothesis as they predict a weak and broad absorption band centered at 328 nm for the $S_0 \rightarrow T_1$. These results suggest that the $S_0 \rightarrow T_1$ transition is possible and significant for NO_3^- photolysis.

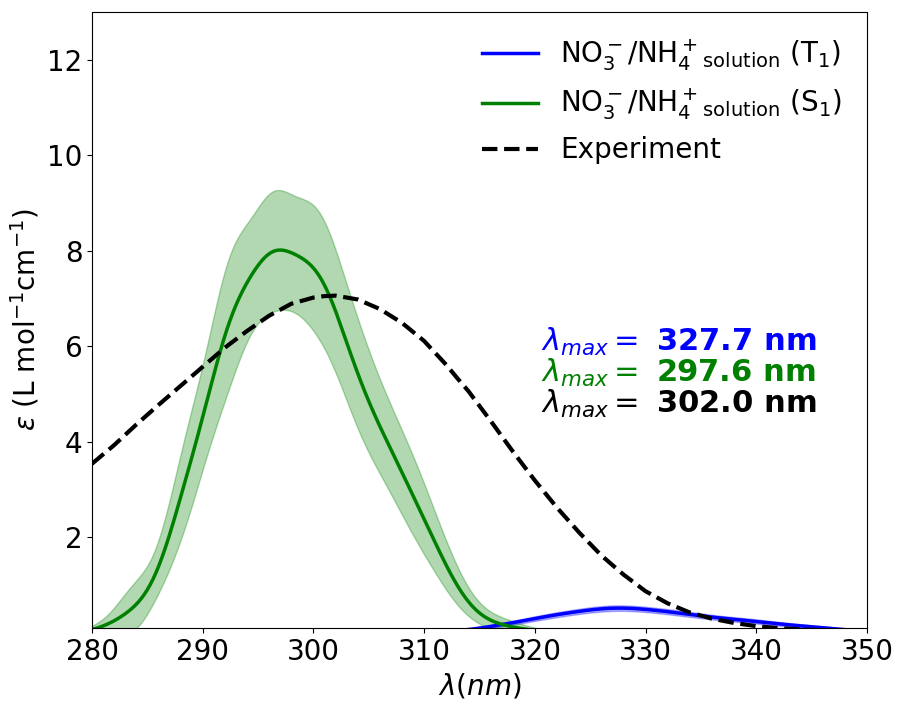


Figure 3: Calculated and experimental UV-visible absorption spectra. The shaded regions correspond to the 95% confidence interval. The 95% confidence interval for the T_1 transition is too small to be visually noticed. The experimental absorption spectrum at 298 K was obtained from the previous work by Chu and Anastasio.¹⁵

Free Energy Surface of NO_3^- (T_1) in Water

Since NO_3^- (T_1) does not dissociate in 2 ps after the vertical excitation to the T_1 state, metadynamics simulations are performed to estimate the dissociation barriers. To assess the reliability of the metadynamics simulation and the choice of CVs - N-O distance, and coordination number of the NO_2 fragment - in the spirit of commitment probability analysis, we run eight unbiased AIMD simulations starting from configurations near the first transition state with randomized velocities. Four of the trajectories return to the initial intact NO_3^- (T_1) state, and the two dissociation channels are observed in the other four trajectories, two for Channel (1) and two for Channel (2). The two channels are clearly distinguished by the second CV, n , with the confirmation of the atomic charges and spin densities by Bader charge analysis (see Figure S4 and Table S2 for details).^{93,94} The multiple-walkers well-tempered metadynamics simulation was run for 52 ps and dissociation along both channels was observed. The metadynamics simulation can be considered reasonably well-converged based on the diffusion of the CVs, recrossings of barriers, and the average error of the relative free energy against time through block analysis.^{84,85} Figure S6 shows that several recrossings among the metastable states have occurred. While Walker 1 has only explored Channel (2), Walker 2 has explored both channels. The block analysis is performed using the last 39 ps (75% of the whole data) of the simulation. The average error of the free energy surface has reached ~ 2 kJ/mol with a block size of 9.5 ps (Figure S7a), and the maximum error is ~ 3 kJ/mol (Figure S7b).

The calculated FES shows 4 basins corresponding to 4 metastable states (Figure 4). To characterize the 4 states, we perform a Bader charge analysis on four frames extracted from the corresponding basins.^{93,94} The result of the Bader charge analysis, including the spin densities, are reported in Table 3. The free energy barriers between pairs of contiguous basins are calculated by minimum energy pathway analysis using the MEPSA software,⁹⁵ and are summarized in Table S3. The results are compatible with the experimental estimates of the activation energies.^{15,31} The initial state A corresponds to the intact NO_3^- (T_1) ($d \sim 1.3$

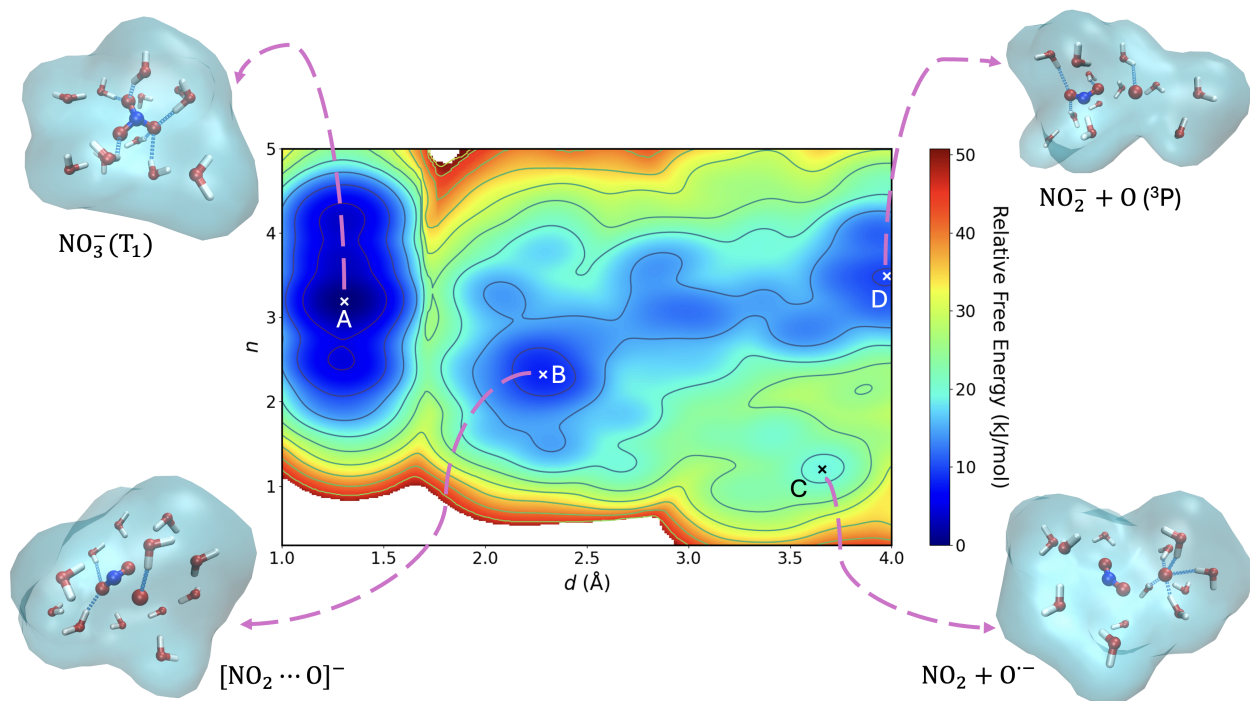


Figure 4: Free energy surface of NO_3^- (T_1) in solution at 300 K. The snapshots of the metastable states are shown with the first two solvation shells (12 water molecules). The intermolecular bonds between the hydrogen atoms of water and the oxygen atoms of NO_3^- are indicated with blue dashed lines if they are within 2.55 Å.

Å, $n \sim 3.2$). In this state, the two unpaired electrons are localized on NO_3^- with Bader charge -0.83 e and spin density 2.0. The system then overcomes a $23 \pm 2\text{ kJ/mol}$ free energy barrier, reaching state B ($d \sim 2.3$, $n \sim 2.3$). The negative charge of state B is neither localized in the NO_2 fragment nor the dissociated O atom. Moreover, atom O1 has a spin density of 1.54, indicating that it is neither O^- nor $\text{O}(^3\text{P})$. This metastable state is a "solvation cage complex" (SCC), $[\text{NO}_2 \cdots \text{O}]^-$, stabilized by hydrogen bonding with water molecules in the first solvation shell, and characterized by the delocalization of the electron in the excited state. Simulations with implicit solvent models cannot capture this effect. The solvation cage effect was formerly hypothesized to be the cause for the low quantum yield of NO_3^- photodissociation in an aqueous solution.²² Our *ab initio* metadynamics simulations uncover the molecular and electronic structure details of the SCC and support this hypothesis. The presence of additional free energy barriers to complete NO_3^- dissociation suggests that the system may remain in the SCC state for a long enough time to enhance the probability

that the photo fragments recombine or deactivate through non-radiative processes. It is worth noting that the N-O distance in the SCC corresponds to the crossover between the T_1 and the S_0 potential energy surfaces in the gas phase (Figure 2). To undergo complete dissociation, the system overcomes either a 16 ± 3 kJ/mol barrier to state C ($d \sim 3.6$, $n \sim 1.2$), which corresponds to Channel (1) ($\text{NO}_2 + \text{O}^-$), or a 7 ± 2 kJ/mol barrier to state D ($d \sim 4.0$, $n \sim 3.5$), which corresponds to Channel (2) ($\text{NO}_2^- + \text{O}({}^3\text{P})$). Bader charge analysis of the products allows us to discriminate the two channels unequivocally, as both in states C and D the excess negative charge is localized on either the NO_2 or the O fragment (Table 3).

Table 3: Bader charge analysis of the 4 metastable states on the free energy surface in Figure 4. The values of the two collective variables (N-O distance d , and coordination number n) correspond to the minima of the metastable states. Each charge and spin density corresponds to the atoms in the parentheses. The spin density corresponds to the total number of unpaired electrons among the atoms.

State	CVs: d (Å), n	Bader Charge (e)	Bader Spin Density
A	1.3, 3.2	-0.83 (NO_3^-)	2.00 (NO_3^-)
B	2.3, 2.3	-0.51 (NO_2) / -0.39 (O)	0.46 (NO_2) / 1.54 (O)
C	3.6, 1.2	-0.00 (NO_2) / -0.72 (O^-)	1.00 (NO_2) / 0.99 (O^-)
D	4.0, 3.5	-0.86 (NO_2^-) / -0.01 ($\text{O}({}^3\text{P})$)	0.01 (NO_2^-) / 1.98 ($\text{O}({}^3\text{P})$)

We note that the free energy barrier from the SCC to $\text{NO}_2 + \text{O}^-$ is about twice as high as the barrier from the SCC to $\text{NO}_2^- + \text{O}({}^3\text{P})$ (Table S3). This difference is related to the rearrangement of hydrogen bonds (H-bonds) in the first solvation shell of the SCC. To ascertain the molecular origin of the features of the FES of dissociation, we have run a set of unbiased trajectories starting from the transition state between states A ($T_1 \text{NO}_3^-$) and B (SCC) (Figure S4). In two of these trajectories (labeled 5 and 6), the system remains in the SCC basin and eventually evolves to form $\text{NO}_2 + \text{O}^-$ [Channel (1)]. In two other trajectories (7 and 8) the system remains in the SCC basin for a shorter time eventually forming $\text{NO}_2^- + \text{O}({}^3\text{P})$ [Channel (2)]. Examining the features of the first solvation shell in these two different cases, we observe that dissociation along Channel (1) involves a substantial reconfiguration of the H-bonds around the two fragments - NO_2 and O^- . The average number of

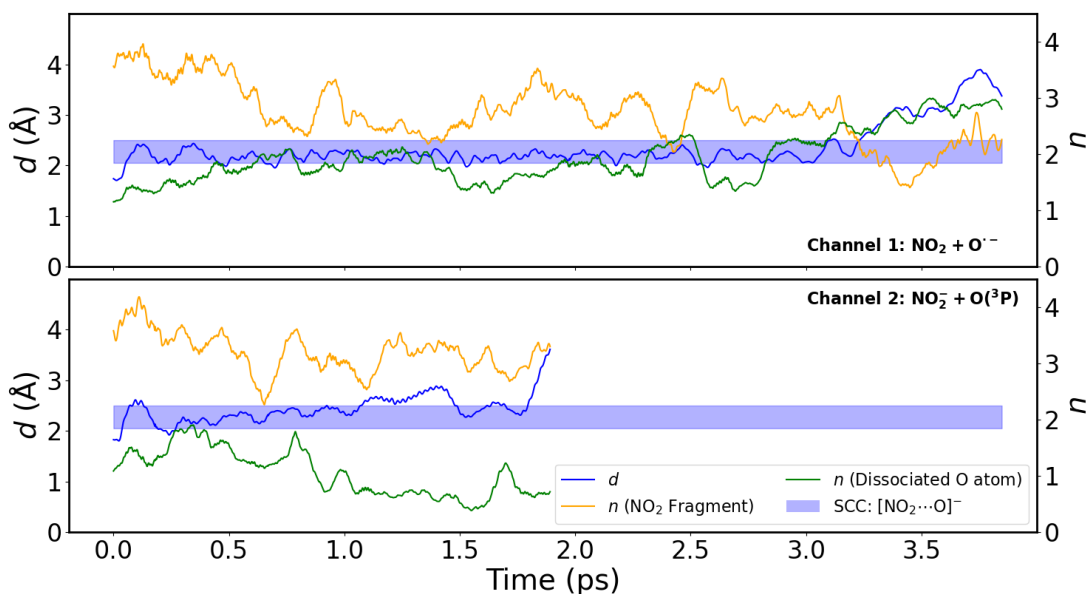


Figure 5: Time evolution of N-O1 distance (d) and the number of H-bonds (n) from the unbiased trajectories 5 and 8 are shown in Figure S4. The blue, orange, and green curves correspond to d , n of the NO_2 fragment, and n of the dissociated O atom, respectively. The shaded region indicates the SCC metastable state.

H-bonds around NO_2 drops from 3.5 to 1.5, whereas the dissociating oxygen increases its coordination with the surrounding water molecules from 1.5 to 2.5 (Figure 5). Conversely, in the trajectory that probes Channel (2) the average number of H-bonds between water and the two fragments - $\text{NO}_2^- + \text{O}({}^3\text{P})$ - does not vary significantly (Figure 5). The different H-bonds rearrangements involved in the two channels account for the longer resident times in the SCC for the unbiased trajectories that evolve along Channel (1) and correlate qualitatively with the higher free energy barrier. It can also qualitatively explain the different temperature dependence of the two channels observed in experiments, indicating that Channel (1) becomes more favorable at high temperatures.²⁷

Quantum Yield Calculations

We employ a master equation five-state model to estimate the quantum yields of both channels after NO_3^- is excited to the T_1 state. The five states comprise the four basins identified

in the T₁ FES and the S₀ ground state of NO₃⁻. Quantum yield is experimentally defined as the fraction of dissociation products over the absorbed photons.^{12,15} In this case, we define it as the fraction of NO₃⁻ in the T₁ state that dissociates into NO₂ or NO₂⁻ normalized by the ratio of the calculated molar absorptivity to the T₁ state to the total molar absorptivity at 313 nm from Figure 3, which is ~ 0.043. Using transition state theory,⁹⁶ we estimate the rate constants from the free energy barriers in Table S3. Additionally, we compute non-radiative rates for intersystem crossings from states A (T₁ NO₃⁻) and B (SCC) to the S₀ ground state using Fermi's golden rule combined with the path integral approach (see section S6).⁸⁶⁻⁸⁸ We also assume that once NO₃⁻ fully dissociates into NO₂ and NO₂⁻ the transition is irreversible, as the fragments will undergo further secondary reactions. The transition rate constants are summarized in Table S5. It is worth noting that starting from NO₃⁻ in the excited T₁ state the transition to the SCC is about 1000 times faster than the de-excitation to the ground state. However, the T₁-S₀ intersystem crossing in the SCC is much more favorable and the deactivation rate is faster than the transition rates to complete dissociation along either Channel (1) or (2). Indeed, the SCC geometry conforms to a minimum energy crossing point between the S₀ and T₁ potential energy surfaces of NO₃⁻ both in the gas phase and in an implicit solvent model (see details of these calculations in SI, Section S6). Under these circumstances, the electronic spin-orbit coupling between the T₁ and S₀ states at the SCC geometry becomes much more significant resulting in a high intersystem crossing rate.

Given the large uncertainties in the calculation of the free energy barriers, we can only predict a range for the photolysis quantum yields, namely 0.01-0.04% for Channel (1) and 0.23-1.25% for Channel (2). The estimated averages are 0.02% and 0.57%, respectively. According to experiments, the two channels in an aqueous solution have similar quantum yields (~ 1%) at room temperature, as the free energy barriers of the two channels are both ~ 11 ± 1 kJ/mol at 300 K.^{15,31} Whereas our estimate for the range of the quantum yield for Channel (2) is compatible with experiments, for Channel (1) it is largely underestimated. Besides the uncertainties on the free energy barriers, due to the limited sampling time, a

possible reason lies in inaccuracies related to the chosen DFT hybrid functional and the lack of nuclear quantum effects. Previous studies suggest that these two effects combined may lead to an overestimate of the melting point of water between 15 and 20 K.⁶⁵ Hence, our model may be considered representative of a solution at about 10 K above the melting point, where the quantum yield for Channel (2) is much larger than for Channel (1).³¹ Another possible reason is that NO_3^- excitations in the S_1 state may also feed Channel (1) through a molecular mechanism similar to that explored in our metadynamics simulations. However, we currently do not have the modeling tools to verify this hypothesis.

Conclusions

Our simulations provide atomistic insights into NO_3^- photolysis in aqueous solution. We have shown that this environmentally significant reaction can occur on the triplet potential energy surface producing either nitrite or NO_2 . This process can be initiated by the direct spin-forbidden transition from the ground state (S_0) to the first triplet state (T_1). Although the transition is \sim 15 times weaker than the spin-allowed transition, this pathway is practically significant when the majority of NO_3^- (S_1) is deactivated non radiatively.³⁵ We also calculated the UV-visible absorption spectra for the two transitions and compared them with the experimental spectrum. The calculated spectra show that the peak for the $S_0 \rightarrow T_1$ transition is hidden within the experimental broad peak. This opens the door for further experimental studies for this direct spin-forbidden excitation.

For the dissociation dynamics after the photoexcitation, we have shown that the necessity of using hybrid density functional to simulate NO_3^- photolysis in an aqueous solution and the capability of multiple walkers well-tempered metadynamics to model its reaction dynamics with explicit solvent molecules at the T_1 state. Both photodissociation channels are observed, and a SCC is identified. This metastable SCC extends the present picture of the solvation cage effect in the community from a microscopic perspective, allowing for an illustration of

how the photo fragments can recombine before escaping from the solvation cage. We also estimate the triplet state quantum yields of the two channels with a master equation model. The results agree qualitatively with experiments in which Channel (2) dominates at a lower temperature. Further investigations on S_1 state dynamics, non-adiabatic interactions, and transitions among electronic states with explicit solvents will help complete the complex picture of NO_3^- photolysis.

The current research provides an example of modeling photochemistry in a bulk aqueous solution, which can provide insight into how photolysis occurs in different pathways. We show that it is necessary to explicitly model the solvation environment with a reliable electronic structure method to explore different chemical reaction pathways. We find that the rearrangement of H-bonds is necessary to illustrate the temperature dependence of the two channels of NO_3^- photolysis under solvation environments, which cannot be observed using an implicit solvent model. To obtain a more comprehensive picture of NO_3^- photolysis under environmental conditions, the current modeling method will be transferred and adapted to investigate NO_3^- photolysis at different environmental surfaces, such as the air-ice interface, and metal oxides.^{30,97}

Conflicts of interest

There are no conflicts to declare.

Supporting Information

The gas-phase calculations, electronic properties of NH_4NO_3 solution, non-spontaneous dissociation of T_1 in solution, unbiased AIMD trajectories in solution from the transition state, error analysis of the multiple walkers well-tempered metadynamics simulation, and the details on the master equation model.

Data availability

Data are available on PLUMED-NEST xxx-xxx.

Acknowledgements

We are grateful to Ted Hullar and Aaron Lieberman for several valuable discussions and suggestions. We thank Wang-Yeuk Kong for useful suggestions on the gas-phase calculations. This work was supported by the National Science Foundation under Grant No. 2305164. This work used the Expanse facility at the San Diego Supercomputer Center through allocation CHE220067 from the Advanced Cyberinfrastructure Coordination Ecosystem: Services and Support (ACCESS) program, which is supported by National Science Foundation grants #2138259, #2138286, #2138307, #2137603, and #2138296.

References

- (1) Jacob, D. J. *Introduction to Atmospheric Chemistry*; Princeton University Press, 1999.
- (2) Seinfeld, J. H.; Pandis, S. N. *Atmospheric Chemistry and Physics: From Air Pollution to Climate Change*; John Wiley & Sons, 2016.
- (3) Cao, Y.; Ma, Q.; Chu, B.; He, H. Homogeneous and heterogeneous photolysis of nitrate in the atmosphere: state of the science, current research needs, and future prospects. *Front. Environ. Sci. Eng.* **2022**, *17*, 48.
- (4) Warneck, P.; Wurzinger, C. Product quantum yields for the 305-nm photodecomposition of nitrate in aqueous solution. *J. Phys. Chem.* **1988**, *92*, 6278–6283.
- (5) Mack, J.; Bolton, J. R. Photochemistry of nitrite and nitrate in aqueous solution: a review. *J. Photochem. Photobiol., A* **1999**, *128*, 1–13.

- (6) Finlayson-Pitts, B. J.; Jr, J. N. P. *Chemistry of the Upper and Lower Atmosphere: Theory, Experiments, and Applications*; Elsevier, 1999.
- (7) Ye, C. et al. Rapid cycling of reactive nitrogen in the marine boundary layer. *Nature* **2016**, *532*, 489–491.
- (8) Reed, C.; Evans, M. J.; Crilley, L. R.; Bloss, W. J.; Sherwen, T.; Read, K. A.; Lee, J. D.; Carpenter, L. J. Evidence for renoxification in the tropical marine boundary layer. *Atmos. Chem. Phys.* **2017**, *17*, 4081–4092.
- (9) Zhu, Y.; Wang, Y.; Zhou, X.; Elshorbany, Y. F.; Ye, C.; Hayden, M.; Peters, A. J. An investigation into the chemistry of HONO in the marine boundary layer at Tudor Hill Marine Atmospheric Observatory in Bermuda. *Atmos. Chem. Phys.* **2022**, *22*, 6327–6346.
- (10) Shah, V. et al. Nitrogen oxides in the free troposphere: implications for tropospheric oxidants and the interpretation of satellite NO₂ measurements. *Atmos. Chem. Phys.* **2023**, *23*, 1227–1257.
- (11) Zhang, R.; Chan, C. K. Simultaneous formation of sulfate and nitrate via co-uptake of SO₂ and NO₂ by aqueous NaCl droplets: combined effect of nitrate photolysis and chlorine chemistry. *Atmos. Chem. Phys.* **2023**, *23*, 6113–6126.
- (12) Benedict, K. B.; McFall, A. S.; Anastasio, C. Quantum Yield of Nitrite from the Photolysis of Aqueous Nitrate above 300 nm. *Environ. Sci. Technol.* **2017**, *51*, 4387–4395.
- (13) Zepp, R. G.; Hoigne, J.; Bader, H. Nitrate-induced photooxidation of trace organic chemicals in water. *Environ. Sci. Technol.* **1987**, *21*, 443–450.
- (14) Zellner, R.; Exner, M.; Herrmann, H. Absolute OH quantum yields in the laser photolysis of nitrate, nitrite and dissolved H₂O₂ at 308 and 351 nm in the temperature range 278–353 K. *J. Atmos. Chem.* **1990**, *10*, 411–425.

- (15) Chu, L.; Anastasio, C. Quantum Yields of Hydroxyl Radical and Nitrogen Dioxide from the Photolysis of Nitrate on Ice. *J. Phys. Chem. A* **2003**, *107*, 9594–9602.
- (16) Chu, L.; Anastasio, C. Temperature and Wavelength Dependence of Nitrite Photolysis in Frozen and Aqueous Solutions. *Environ. Sci. Technol.* **2007**, *41*, 3626–3632.
- (17) Scharko, N. K.; Berke, A. E.; Raff, J. D. Release of Nitrous Acid and Nitrogen Dioxide from Nitrate Photolysis in Acidic Aqueous Solutions. *Environ. Sci. Technol.* **2014**, *48*, 11991–12001.
- (18) Noyes, R. M. Kinetics of Competitive Processes when Reactive Fragments are Produced in Pairs. *J. Am. Chem. Soc.* **1955**, *77*, 2042–2045.
- (19) Noyes, R. M. Models Relating Molecular Reactivity and Diffusion in Liquids. *J. Am. Chem. Soc.* **1956**, *78*, 5486–5490.
- (20) Nissenson, P.; Knox, C. J. H.; Finlayson-Pitts, B. J.; Phillips, L. F.; Dabdub, D. Enhanced photolysis in aerosols: evidence for important surface effects. *Phys. Chem. Chem. Phys.* **2006**, *8*, 4700.
- (21) Davis, D.; Seelig, J.; Huey, G.; Crawford, J.; Chen, G.; Wang, Y.; Buhr, M.; Helmig, D.; Neff, W.; Blake, D. A reassessment of Antarctic plateau reactive nitrogen based on ANTCI 2003 airborne and ground based measurements. *Atmos. Environ.* **2008**, *42*, 2831–2848.
- (22) Nissenson, P.; Dabdub, D.; Das, R.; Maurino, V.; Minero, C.; Vione, D. Evidence of the water-cage effect on the photolysis of NO_3^- and FeOH^{2+} . Implications of this effect and of H_2O_2 surface accumulation on photochemistry at the air–water interface of atmospheric droplets. *Atmos. Environ.* **2010**, *44*, 4859–4866.
- (23) Richards, N. K.; Wingen, L. M.; Callahan, K. M.; Nishino, N.; Kleinman, M. T.;

- Tobias, D. J.; Finlayson-Pitts, B. J. Nitrate Ion Photolysis in Thin Water Films in the Presence of Bromide Ions. *J. Phys. Chem. A* **2011**, *115*, 5810–5821.
- (24) Meusinger, C.; Berhanu, T. A.; Erbland, J.; Savarino, J.; Johnson, M. S. Laboratory study of nitrate photolysis in Antarctic snow. I. Observed quantum yield, domain of photolysis, and secondary chemistry. *J. Chem. Phys.* **2014**, *140*, 244305.
- (25) Marcotte, G.; Marchand, P.; Pronovost, S.; Ayotte, P.; Laffon, C.; Parent, P. Surface-Enhanced Nitrate Photolysis on Ice. *J. Phys. Chem. A* **2015**, *119*, 1996–2005.
- (26) McFall, A. S.; Edwards, K. C.; Anastasio, C. Nitrate Photochemistry at the Air–Ice Interface and in Other Ice Reservoirs. *Environ. Sci. Technol.* **2018**, *52*, 5710–5717.
- (27) Hullar, T.; Tran, T.; Anastasio, C. Nitrate Photolysis at the Air–Ice Interface of Nature-Identical Snow. *ACS Earth Space Chem.* **2023**, *7*, 1791–1797.
- (28) Berrens, M. L.; Chen, Z.; Chan, K.-T.; Anastasio, C.; Donadio, D. Solvation Structure and UV–Visible Absorption Spectra of the Nitrate Anion at the Air–Ice Interface by First-Principles Molecular Simulations. *ACS Earth Space Chem.* **2023**, *7*, 1761–1769.
- (29) Bononi, F. C.; Chen, Z.; Rocca, D.; Andreussi, O.; Hullar, T.; Anastasio, C.; Donadio, D. Bathochromic Shift in the UV–Visible Absorption Spectra of Phenols at Ice Surfaces: Insights from First-Principles Calculations. *J. Phys. Chem. A* **2020**, *124*, 9288–9298.
- (30) Hullar, T.; Tran, T.; Chen, Z.; Bononi, F.; Palmer, O.; Donadio, D.; Anastasio, C. Enhanced photodegradation of dimethoxybenzene isomers in/on ice compared to in aqueous solution. *Atmos. Chem. Phys.* **2022**, *22*, 5943–5959.
- (31) Benedict, K. B.; Anastasio, C. Quantum Yields of Nitrite (NO_2^-) from the Photolysis of Nitrate (NO_3^-) in Ice at 313 nm. *J. Phys. Chem. A* **2017**, *121*, 8474–8483, Publisher: American Chemical Society.

- (32) de Jesus Medeiros, D.; Pimentel, A. S. New Insights in the Atmospheric HONO Formation: New Pathways for N₂O₄ Isomerization and NO₂ Dimerization in the Presence of Water. *J. Phys. Chem. A* **2011**, *115*, 6357–6365.
- (33) Harris, L. E. The lower electronic states of nitrite and nitrate ion, nitromethane, nitramide, nitric acid, and nitrate esters. *J. Chem. Phys.* **1973**, *58*, 5615–5626.
- (34) Svoboda, O.; Kubelová, L.; Slavíček, P. Enabling Forbidden Processes: Quantum and Solvation Enhancement of Nitrate Anion UV Absorption. *J. Phys. Chem. A* **2013**, *117*, 12868–12877.
- (35) Svoboda, O.; Slavíček, P. Is Nitrate Anion Photodissociation Mediated by Singlet–Triplet Absorption? *J. Phys. Chem. Lett.* **2014**, *5*, 1958–1962.
- (36) Pedersen, P. D.; Rasmussen, M. H.; Mikkelsen, K. V.; Johnson, M. S. The riddle of the forbidden UV absorption of aqueous nitrate: the oscillator strength of the n → π* transition in NO₃⁻ including second order vibronic coupling. *Phys. Chem. Chem. Phys.* **2019**, *21*, 23466–23472.
- (37) Pedersen, P. D.; Mikkelsen, K. V.; Johnson, M. S. The unexpected effect of aqueous ion pairs on the forbidden n → π* transition in nitrate. *Phys. Chem. Chem. Phys.* **2020**, *22*, 11678–11685.
- (38) Weaver, A.; Arnold, D. W.; Bradforth, S. E.; Neumark, D. M. Examination of the ²A'₂ and ²E" states of NO₃ by ultraviolet photoelectron spectroscopy of NO₃⁻. *J. Chem. Phys.* **1991**, *94*, 1740–1751.
- (39) Wang, X.-B.; Yang, X.; Wang, L.-S.; Nicholas, J. B. Photodetachment and theoretical study of free and water-solvated nitrate anions, NO₃⁻(H₂O_n) (n = 0 – 6). *J. Chem. Phys.* **2002**, *116*, 561–570.

- (40) Fehér, P. P.; Madarász, Á.; Stirling, A. Multiscale Modeling of Electronic Spectra Including Nuclear Quantum Effects. *J. Chem. Theory Comput.* **2021**, *17*, 6340–6352.
- (41) Timrov, I.; Andreussi, O.; Biancardi, A.; Marzari, N.; Baroni, S. Self-consistent continuum solvation for optical absorption of complex molecular systems in solution. *J. Chem. Phys.* **2015**, *142*, 034111.
- (42) Iannuzzi, M.; Laio, A.; Parrinello, M. Efficient Exploration of Reactive Potential Energy Surfaces Using Car-Parrinello Molecular Dynamics. *Phys. Rev. Lett.* **2003**, *90*, 238302.
- (43) Barducci, A.; Bussi, G.; Parrinello, M. Well-Tempered Metadynamics: A Smoothly Converging and Tunable Free-Energy Method. *Phys. Rev. Lett.* **2008**, *100*, 020603.
- (44) Barducci, A.; Bonomi, M.; Parrinello, M. Metadynamics. *WIREs Comput. Mol. Sci.* **2011**, *1*, 826–843.
- (45) Angeli, C.; Cimiraglia, R.; Evangelisti, S.; Leininger, T.; Malrieu, J.-P. Introduction of n -electron valence states for multireference perturbation theory. *J. Chem. Phys.* **2001**, *114*, 10252–10264.
- (46) Angeli, C.; Borini, S.; Cestari, M.; Cimiraglia, R. A quasidegenerate formulation of the second order n-electron valence state perturbation theory approach. *J. Chem. Phys.* **2004**, *121*, 4043–4049.
- (47) Soda, T.; Kitagawa, Y.; Onishi, T.; Takano, Y.; Shigeta, Y.; Nagao, H.; Yoshioka, Y.; Yamaguchi, K. Ab initio computations of effective exchange integrals for H–H, H–He–H and Mn₂O₂ complex: comparison of broken-symmetry approaches. *Chem. Phys. Lett.* **2000**, *319*, 223–230.
- (48) Yanai, T.; Tew, D. P.; Handy, N. C. A new hybrid exchange–correlation functional using the Coulomb-attenuating method (CAM-B3LYP). *Chem. Phys. Lett.* **2004**, *393*, 51–57.

- (49) Zheng, J.; Xu, X.; Truhlar, D. G. Minimally augmented Karlsruhe basis sets. *Theor. Chem. Acc.* **2011**, *128*, 295–305.
- (50) Werner, H.-J.; Knowles, P. J. A second order multiconfiguration SCF procedure with optimum convergence. *J. Chem. Phys.* **1985**, *82*, 5053–5063.
- (51) Angeli, C.; Cimiraglia, R.; Malrieu, J.-P. N-electron valence state perturbation theory: a fast implementation of the strongly contracted variant. *Chem. Phys. Lett.* **2001**, *350*, 297–305.
- (52) Lang, L.; Sivalingam, K.; Neese, F. The combination of multipartitioning of the Hamiltonian with canonical Van Vleck perturbation theory leads to a Hermitian variant of quasidegenerate N-electron valence perturbation theory. *J. Chem. Phys.* **2020**, *152*, 014109.
- (53) Dunning, T. H. Gaussian basis sets for use in correlated molecular calculations. I. The atoms boron through neon and hydrogen. *J. Chem. Phys.* **1989**, *90*, 1007–1023.
- (54) Langhoff, S. R.; Davidson, E. R. Configuration interaction calculations on the nitrogen molecule. *Int. J. Quantum Chem.* **1974**, *8*, 61–72.
- (55) Zhang, Y.; Yang, W. Comment on “Generalized Gradient Approximation Made Simple”. *Phys. Rev. Lett.* **1998**, *80*, 890–890.
- (56) Adamo, C.; Barone, V. Toward reliable density functional methods without adjustable parameters: The PBE0 model. *J. Chem. Phys.* **1999**, *110*, 6158–6170.
- (57) Grimme, S.; Antony, J.; Ehrlich, S.; Krieg, H. A consistent and accurate *ab initio* parametrization of density functional dispersion correction (DFT-D) for the 94 elements H–Pu. *J. Chem. Phys.* **2010**, *132*, 154104.
- (58) Weigend, F.; Ahlrichs, R. Balanced basis sets of split valence, triple zeta valence and

- quadruple zeta valence quality for H to Rn: Design and assessment of accuracy. *Phys. Chem. Chem. Phys.* **2005**, *7*, 3297–3305.
- (59) Weigend, F. Accurate Coulomb-fitting basis sets for H to Rn. *Phys. Chem. Chem. Phys.* **2006**, *8*, 1057–1065.
- (60) Marenich, A. V.; Cramer, C. J.; Truhlar, D. G. Universal Solvation Model Based on Solute Electron Density and on a Continuum Model of the Solvent Defined by the Bulk Dielectric Constant and Atomic Surface Tensions. *J. Phys. Chem. B* **2009**, *113*, 6378–6396.
- (61) Neese, F.; Wennmohs, F.; Becker, U.; Ripplinger, C. The ORCA quantum chemistry program package. *J. Chem. Phys.* **2020**, *152*, 224108.
- (62) VandeVondele, J.; Krack, M.; Mohamed, F.; Parrinello, M.; Chassaing, T.; Hutter, J. Quickstep: Fast and accurate density functional calculations using a mixed Gaussian and plane waves approach. *Comput. Phys. Commun.* **2005**, *167*, 103–128.
- (63) Kühne, T. D. et al. CP2K: An electronic structure and molecular dynamics software package - Quickstep: Efficient and accurate electronic structure calculations. *J. Chem. Phys.* **2020**, *152*, 194103.
- (64) Cheng, B.; Engel, E. A.; Behler, J.; Dellago, C.; Ceriotti, M. Ab initio thermodynamics of liquid and solid water. *Proc. Natl. Acad. Sci. U.S.A.* **2019**, *116*, 1110–1115.
- (65) Chen, Z.; Berrens, M. L.; Chan, K.-T.; Fan, Z.; Donadio, D. Thermodynamics of Water and Ice from a Fast and Scalable First-Principles Neuroevolution Potential. *J. Chem. Eng. Data* **2024**, *69*, 128–140.
- (66) VandeVondele, J.; Hutter, J. Gaussian basis sets for accurate calculations on molecular systems in gas and condensed phases. *J. Chem. Phys.* **2007**, *127*, 114105.

- (67) Guidon, M.; Hutter, J.; VandeVondele, J. Auxiliary Density Matrix Methods for Hartree—Fock Exchange Calculations. *J. Chem. Theory Comput.* **2010**, *6*, 2348–2364.
- (68) Goedecker, S.; Teter, M.; Hutter, J. Separable dual-space Gaussian pseudopotentials. *Phys. Rev. B* **1996**, *54*, 1703–1710.
- (69) Bussi, G.; Donadio, D.; Parrinello, M. Canonical sampling through velocity rescaling. *J. Chem. Phys.* **2007**, *126*, 014101.
- (70) Riikonen, S.; Parkkinen, P.; Halonen, L.; Gerber, R. B. Ionization of Acids on the Quasi-Liquid Layer of Ice. *J. Phys. Chem. A* **2014**, *118*, 5029–5037.
- (71) Gerber, R. B.; Varner, M. E.; Hammerich, A. D.; Riikonen, S.; Murdachaew, G.; Shemesh, D.; Finlayson-Pitts, B. J. Computational Studies of Atmospherically-Relevant Chemical Reactions in Water Clusters and on Liquid Water and Ice Surfaces. *Acc. Chem. Res.* **2015**, *48*, 399–406.
- (72) de la Puente, M.; David, R.; Gomez, A.; Laage, D. Acids at the Edge: Why Nitric and Formic Acid Dissociations at Air–Water Interfaces Depend on Depth and on Interface Specific Area. *J. Am. Chem. Soc.* **2022**, *144*, 10524–10529.
- (73) Perdew, J. P.; Burke, K.; Ernzerhof, M. Generalized Gradient Approximation Made Simple. *Phys. Rev. Lett.* **1996**, *77*, 3865–3868.
- (74) Gaiduk, A. P.; Zhang, C.; Gygi, F.; Galli, G. Structural and electronic properties of aqueous NaCl solutions from ab initio molecular dynamics simulations with hybrid density functionals. *Chem. Phys. Lett.* **2014**, *604*, 89–96.
- (75) Gaiduk, A. P.; Govoni, M.; Seidel, R.; Skone, J. H.; Winter, B.; Galli, G. Photoelectron Spectra of Aqueous Solutions from First Principles. *J. Am. Chem. Soc.* **2016**, *138*, 6912–6915.

- (76) de Almeida, J. M.; Nguyen, N. L.; Colonna, N.; Chen, W.; Rodrigues Miranda, C.; Pasquarello, A.; Marzari, N. Electronic Structure of Water from Koopmans-Compliant Functionals. *J. Chem. Theory Comput.* **2021**, *17*, 3923–3930.
- (77) Berrens, M. L.; Kundu, A.; Calegari Andrade, M. F.; Pham, T. A.; Galli, G.; Donadio, D. Nuclear Quantum Effects on the Electronic Structure of Water and Ice. *J. Phys. Chem. Lett.* **2024**, *15*, 6818–6825.
- (78) Goerigk, L.; Grimme, S. A thorough benchmark of density functional methods for general main group thermochemistry, kinetics, and noncovalent interactions. *Phys. Chem. Chem. Phys.* **2011**, *13*, 6670.
- (79) Moellmann, J.; Grimme, S. DFT-D3 Study of Some Molecular Crystals. *J. Phys. Chem. C* **2014**, *118*, 7615–7621.
- (80) Barone, V.; Cossi, M. Quantum Calculation of Molecular Energies and Energy Gradients in Solution by a Conductor Solvent Model. *J. Phys. Chem. A* **1998**, *102*, 1995–2001.
- (81) Roemelt, M.; Maganas, D.; DeBeer, S.; Neese, F. A combined DFT and restricted open-shell configuration interaction method including spin-orbit coupling: Application to transition metal L-edge X-ray absorption spectroscopy. *J. Chem. Phys.* **2013**, *138*, 204101.
- (82) Murdachaew, G.; Varner, M. E.; Phillips, L. F.; Finlayson-Pitts, B. J.; Gerber, R. B. Nitrogen dioxide at the air–water interface: trapping, absorption, and solvation in the bulk and at the surface. *Phys. Chem. Chem. Phys.* **2013**, *15*, 204–212.
- (83) Raiteri, P.; Laio, A.; Gervasio, F. L.; Micheletti, C.; Parrinello, M. Efficient Reconstruction of Complex Free Energy Landscapes by Multiple Walkers Metadynamics. *J. Phys. Chem. B* **2006**, *110*, 3533–3539.

- (84) Tiwary, P.; Parrinello, M. A Time-Independent Free Energy Estimator for Metadynamics. *J. Phys. Chem. B* **2015**, *119*, 736–742.
- (85) Tribello, G. A.; Bonomi, M.; Branduardi, D.; Camilloni, C.; Bussi, G. PLUMED 2: New feathers for an old bird. *Comput. Phys. Commun.* **2014**, *185*, 604–613.
- (86) de Souza, B.; Farias, G.; Neese, F.; Izsák, R. Predicting Phosphorescence Rates of Light Organic Molecules Using Time-Dependent Density Functional Theory and the Path Integral Approach to Dynamics. *J. Chem. Theory Comput.* **2019**, *15*, 1896–1904.
- (87) de Souza, B.; Neese, F.; Izsák, R. On the theoretical prediction of fluorescence rates from first principles using the path integral approach. *J. Chem. Phys.* **2018**, *148*, 034104.
- (88) Baiardi, A.; Bloino, J.; Barone, V. General Time Dependent Approach to Vibronic Spectroscopy Including Franck–Condon, Herzberg–Teller, and Duschinsky Effects. *J. Chem. Theory Comput.* **2013**, *9*, 4097–4115.
- (89) Penfold, T. J.; Gindensperger, E.; Daniel, C.; Marian, C. M. Spin-Vibronic Mechanism for Intersystem Crossing. *Chem. Rev.* **2018**, *118*, 6975–7025.
- (90) Veys, K.; Bousquet, M. H. E.; Jacquemin, D.; Escudero, D. Modeling the Fluorescence Quantum Yields of Aromatic Compounds: Benchmarking the Machinery to Compute Intersystem Crossing Rates. *J. Chem. Theory Comput.* **2023**, *19*, 9344–9357.
- (91) Rotlevi, E.; Treinin, A. The 300-m μ Band of NO₃⁻. *J. Phys. Chem.* **1965**, *69*, 2645–2648.
- (92) Mewes, J.-M.; Jerabek, P.; Bohle, D. S.; Schwerdtfeger, P. The Light-Driven Isomerization of Aqueous Nitrate: A Theoretical Perspective. *ChemPhotoChem* **2018**, *2*, 725–733.
- (93) Bader, R. F. W. Atoms in molecules. *Acc. Chem. Res.* **1985**, *18*, 9–15.
- (94) Tang, W.; Sanville, E.; Henkelman, G. A grid-based Bader analysis algorithm without lattice bias. *J. Phys.: Condens. Matter* **2009**, *21*, 084204.

- (95) Marcos-Alcalde, I.; Setoain, J.; Mendieta-Moreno, J. I.; Mendieta, J.; Gómez-Puertas, P. MEPSA: minimum energy pathway analysis for energy landscapes. *Bioinformatics* **2015**, *31*, 3853–3855.
- (96) Hänggi, P.; Talkner, P.; Borkovec, M. Reaction-rate theory: fifty years after Kramers. *Rev. Mod. Phys.* **1990**, *62*, 251–341.
- (97) Rubasinghege, G.; Grassian, V. H. Photochemistry of Adsorbed Nitrate on Aluminum Oxide Particle Surfaces. *J. Phys. Chem. A* **2009**, *113*, 7818–7825.

Supporting Information

Revealing the Photochemical Pathways of Nitrate in Water through First-Principles Simulations

Kam-Tung Chan¹, Margaret L. Berrens¹, Zekun Chen¹, Cort Anastasio², and Davide Donadio¹

¹ Department of Chemistry, University of California Davis, One Shields Ave. Davis, CA, 95616.

² Department of Land, Air, and Water Resources, University of California Davis, One Shields Ave. Davis, CA, 95616.

E-mail: ddonadio@ucdavis.edu

S1: Quantum Chemical Calculations in the Gas Phase and Under Implicit Solvation

The vertical excitation energies of gas phase NO_3^- at its equilibrium geometry are calculated at the level of QD-NEVPT2(10,9)/aug-cc-pVTZ and MRCI+Q(10,9)/aug-cc-pVTZ. The energies of neutral NO_3^\cdot are calculated at the level of QD-NEVPT2(9,9)/aug-cc-pVTZ and MRCI+Q(9,9)/aug-cc-pVTZ. The electron detachment energies are calculated by the difference between the ground state of neutral NO_3^\cdot and the ground state of NO_3^- .

We also performed potential energy surface scans on the ground state and the T_1 states at the level of DFT with implicit solvent models. For the ground state, broken-symmetry DFT was used to optimize the structures. For the T_1 state, the energies were calculated on the ground state structures with an unrestricted Kohn-Sham reference. The solvation model based on density (SMD) of water was used as the implicit solvation model. All these calculations were calculated using the revPBE0 functional with D3 dispersion correction with zero-damping and def2-SVP basis set.

Table S1: The vertical excitation energies of gas phase NO_3^- .

Transition	QD-NEVPT2(10,9)/aug-cc-pVTZ (eV)	MRCI+Q(10,9)/aug-cc-pVTZ (eV)
$S_0 \rightarrow T_1$	4.179	3.626
$S_0 \rightarrow S_1$	4.418	3.808
$S_0 \rightarrow T_2$	5.265	4.632
$S_0 \rightarrow T_3$	5.268	5.089
$S_0 \rightarrow T_4$	5.553	5.091
$S_0 \rightarrow S_2$	5.616	4.714
$\text{NO}_3^- \rightarrow \text{NO}_3^\cdot$	4.379	3.901

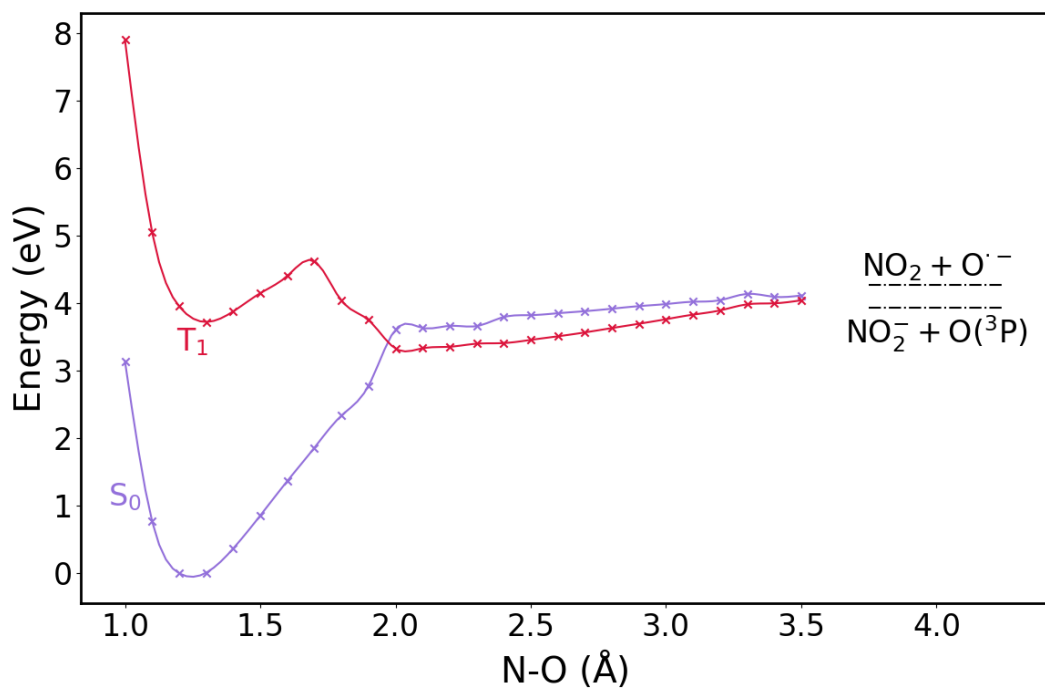


Figure S1: The potential energy curves of NO_3^- calculated at the level of revPBE0-D3/def2-SVP with SMD implicit solvation model of water. The total energies of the isolated species after dissociation are shown in dashed lines

S2: Electronic Properties of NH₄NO₃ Solution

To illustrate the necessity of using hybrid density functional instead of semi-local density functional when performing AIMD simulations at the T₁ state, the projected density of states (PDOS) of NO₃⁻ and water in the NH₄NO₃ solution were calculated and shown in Figure S2. All PDOS were calculated by extracting 200 frames from a preliminary AIMD simulation at the level of a semi-local density functional with dispersion correction (PBE-D3), followed by single point calculations for the energy levels at the S₀ and T₁ state with PBE-D3 and revPBE0-D3, respectively. A previous study has shown that the electronic properties of NaCl and Cl⁻ aqueous solution do not change significantly, regardless of the method of the AIMD simulations. [1] For the case of PBE-D3, as shown in Figure S2a, when the system is vertically excited from S₀ to T₁, the highest occupied molecular orbital (HOMO) of the system, i.e. the unpaired electron of NO₃⁻ is excited near to the edge of the water conduction band. This causes the electron to be delocalized to the water molecules and spontaneous dissociation of NO₃⁻ along the channel (1). Conversely, as shown in Figure S2b, the direct spin-forbidden excitation at the level of revPBE0-D3 excites the unpaired electron to the middle of the water band gap. The unpaired electron remains localized in NO₃⁻, so channel (2) becomes viable in the AIMD simulations. The results above suggest that the substrate and its solvation environment must be accurately modeled to simulate the physics and chemistry of the system of interest. In the current study, hybrid density functional is a more appropriate approach to model the reaction dynamics at its excited state despite its high computational cost.

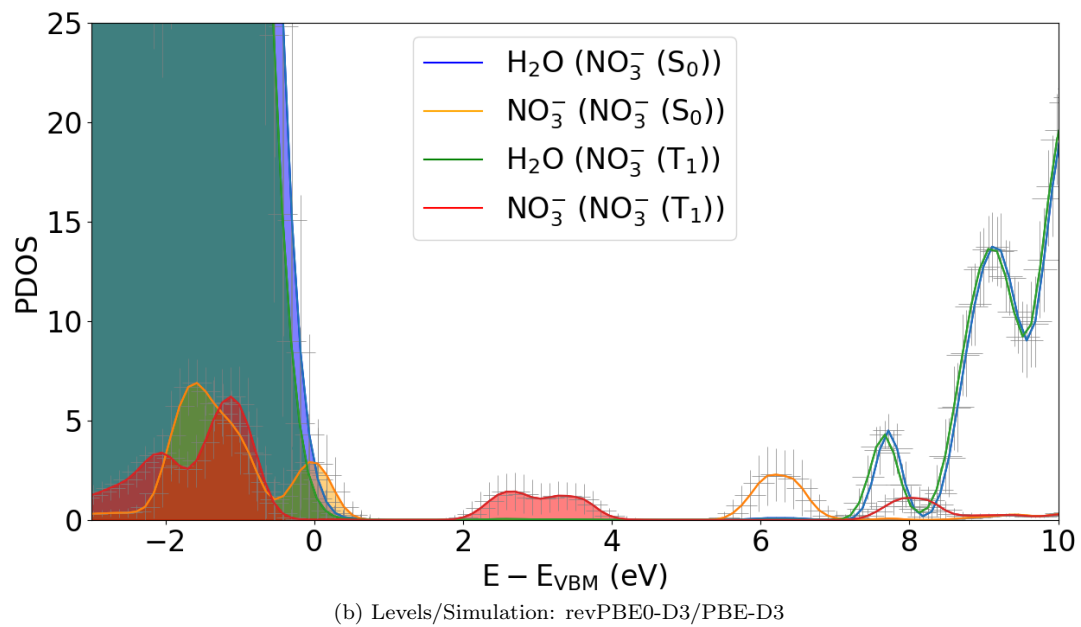
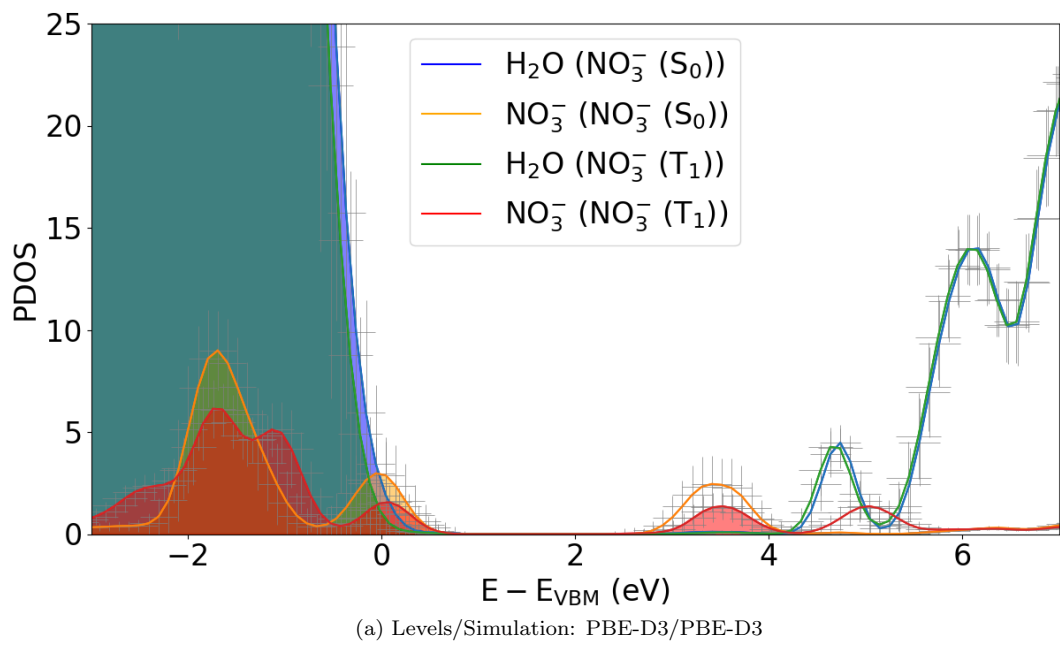


Figure S2: Projected density of states (PDOS) of NO_3^- and water in a NH_4NO_3 solution calculated at the level of (a) PBE-D3/PBE-D3 and (b) revPBE0-D3/PBE-D3. The reference energy is set at the valence band maximum (VBM). NO_3^- and water at the S_0 state are colored in orange and blue respectively, while NO_3^- and water at the T_1 state are colored in red and green respectively. Occupied states are shaded with the corresponding color.

S3: Non-spontaneous Dissociation of NO_3^- (T_1) in Solution After the Vertical Excitation from the S_0 state.

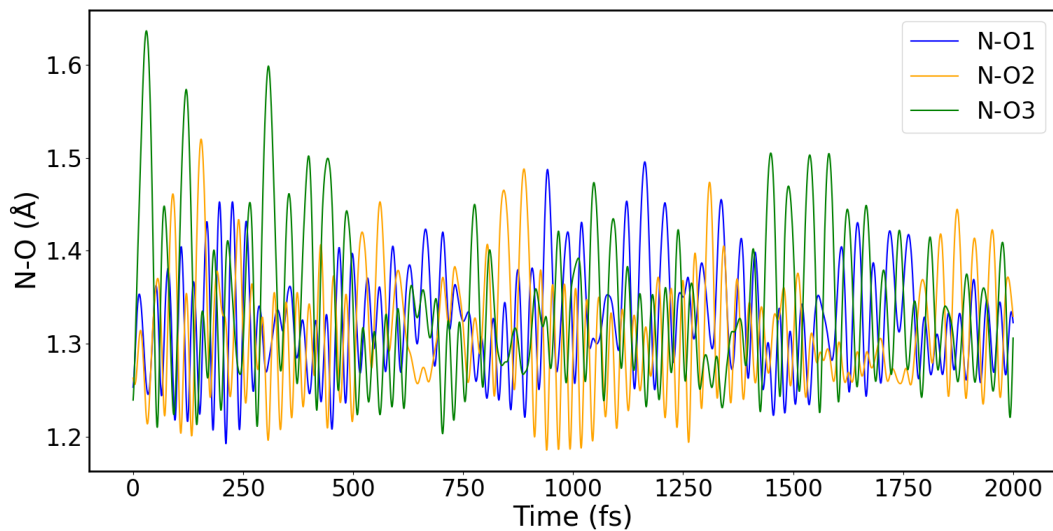


Figure S3: The time evolution of the three N-O bonds in NO_3^- (T_1) after the vertical excitation from the S_0 state.

S4: Unbiased AIMD Trajectories in Solution from the Transition State

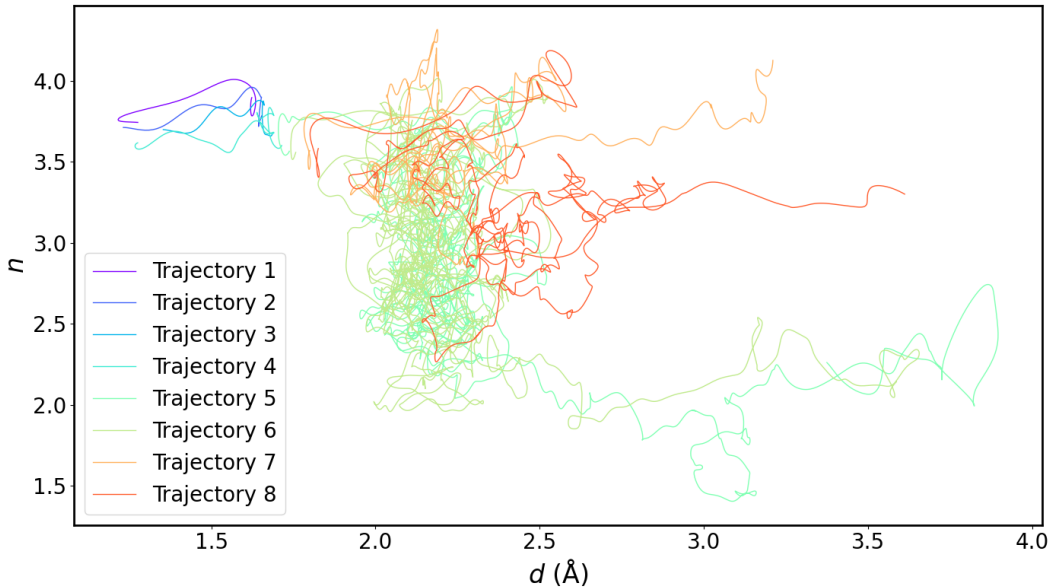


Figure S4: The evolution of the two proposed CVs for each downhill unbiased trajectory starting near the transition state. Trajectories 1 to 4 go back to intact NO_3^- (T_1). Trajectories 5 and 6 go to channel (1). Trajectories 7 and 8 go to channel (2).

Table S2: The Bader charge analysis of the last frame from each trajectory shown in Figure S4. Each charge and spin density corresponds to the species in the parentheses. The spin density corresponds to the total number of unpaired electrons among the atoms.

Trajectory	Bader Charge	Bader Spin Density
1	-0.87 (NO_3^- (T_1))	1.99 (NO_3^- (T_1))
2	-0.87 (NO_3^- (T_1))	1.99 (NO_3^- (T_1))
3	-0.87 (NO_3^- (T_1))	1.99 (NO_3^- (T_1))
4	-0.90 (NO_3^- (T_1))	1.99 (NO_3^- (T_1))
5	-0.01 (NO_2) / -0.75 ($\text{O}^{\bullet-}$)	0.99 (NO_2) / 1.00 ($\text{O}^{\bullet-}$)
6	-0.01 (NO_2) / -0.76 ($\text{O}^{\bullet-}$)	0.98 (NO_2) / 0.97 ($\text{O}^{\bullet-}$)
7	-0.83 (NO_2^-) / -0.02 ($\text{O} (^3\text{P})$)	0.03 (NO_2^-) / 1.96 ($\text{O} (^3\text{P})$)
8	-0.86 (NO_2^-) / -0.01 ($\text{O} (^3\text{P})$)	0.01 (NO_2^-) / 1.98 ($\text{O} (^3\text{P})$)

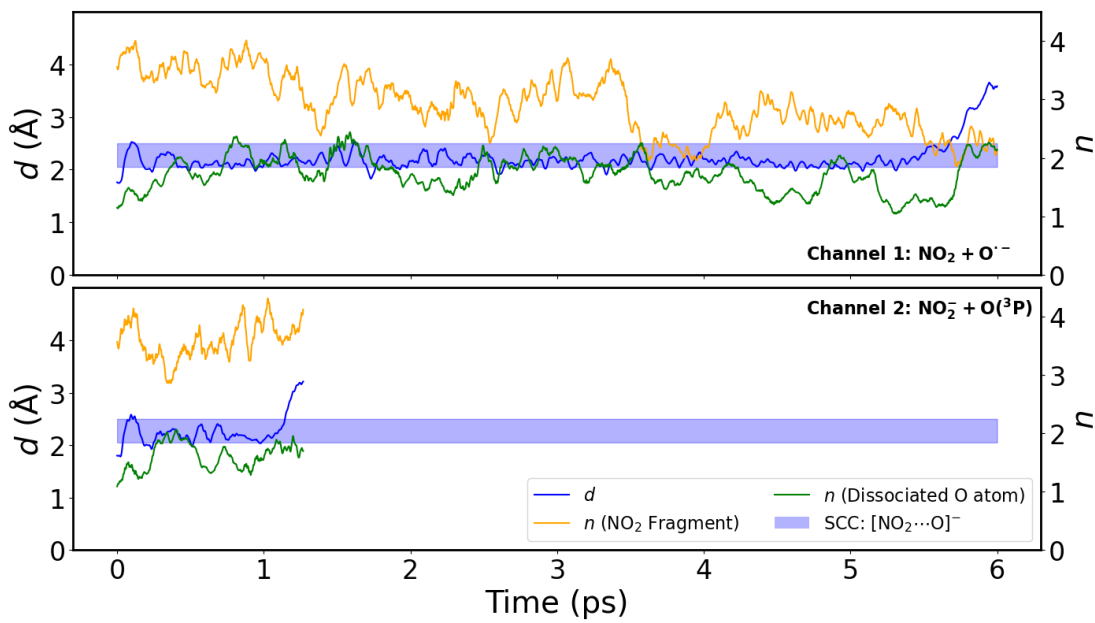


Figure S5: The time evolution of N-O1 distance (d) and the number of H-bonds (n) from the unbiased trajectory 6 and 7 shown in Figure S3. The blue, orange, and green curves correspond to d , n of the NO_2 fragment, and n of the dissociated O atom, respectively. The shaded region indicates the SCC metastable state.

S5: Error Analysis of the Multiple Walkers Well-Tempered Meta-dynamics Simulation

Table S3: The free energy barriers between the 4 meta-stable states on the free energy surface.

Transition	Molecular Fragments	Free Energy Barrier (kJ/mol)
A→B	$\text{NO}_3^-(\text{T}_1) \rightarrow [\text{NO}_2 \cdots \text{O}]^-(\text{T}_1)$	23 ± 2
B→A	$[\text{NO}_2 \cdots \text{O}]^-(\text{T}_1) \rightarrow \text{NO}_3^-(\text{T}_1)$	13 ± 2
B→C	$[\text{NO}_2 \cdots \text{O}]^-(\text{T}_1) \rightarrow \text{NO}_2 + \text{O}^{\bullet-}$	16 ± 3
B→D	$[\text{NO}_2 \cdots \text{O}]^-(\text{T}_1) \rightarrow \text{NO}_2^- + \text{O } (^3\text{P})$	7 ± 3

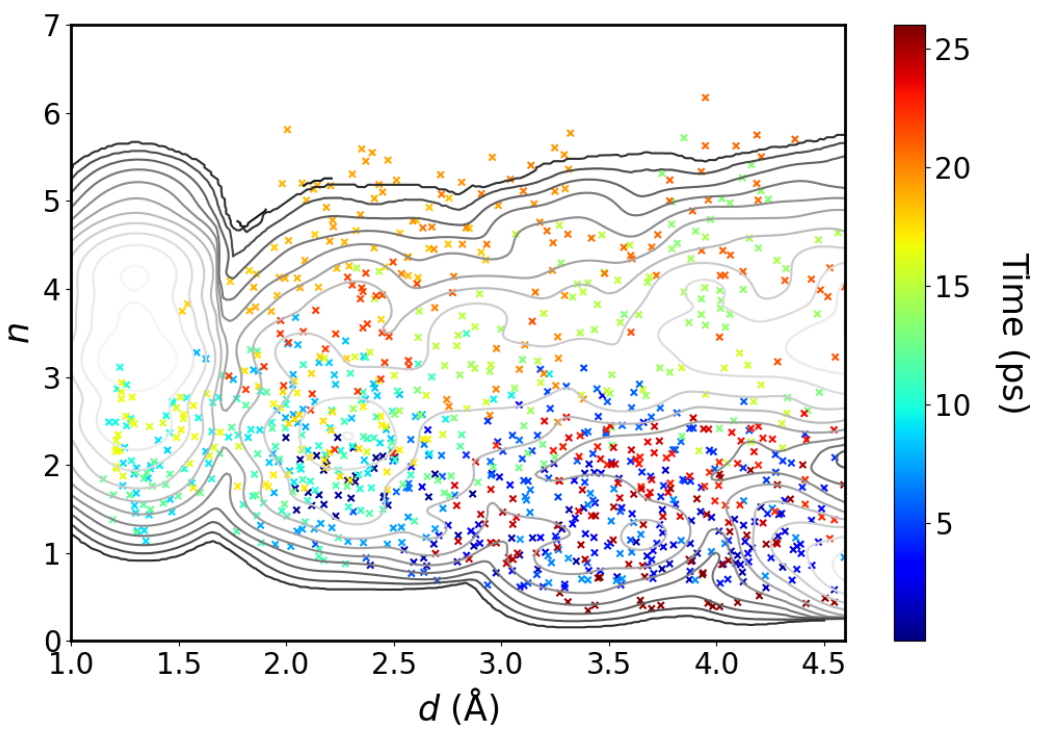
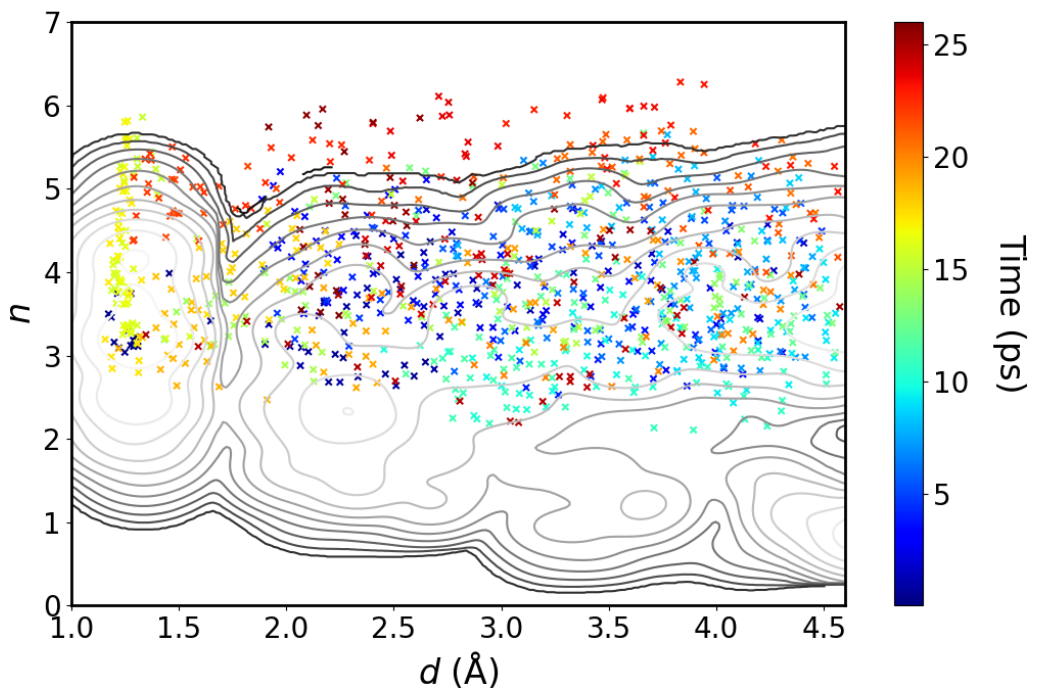
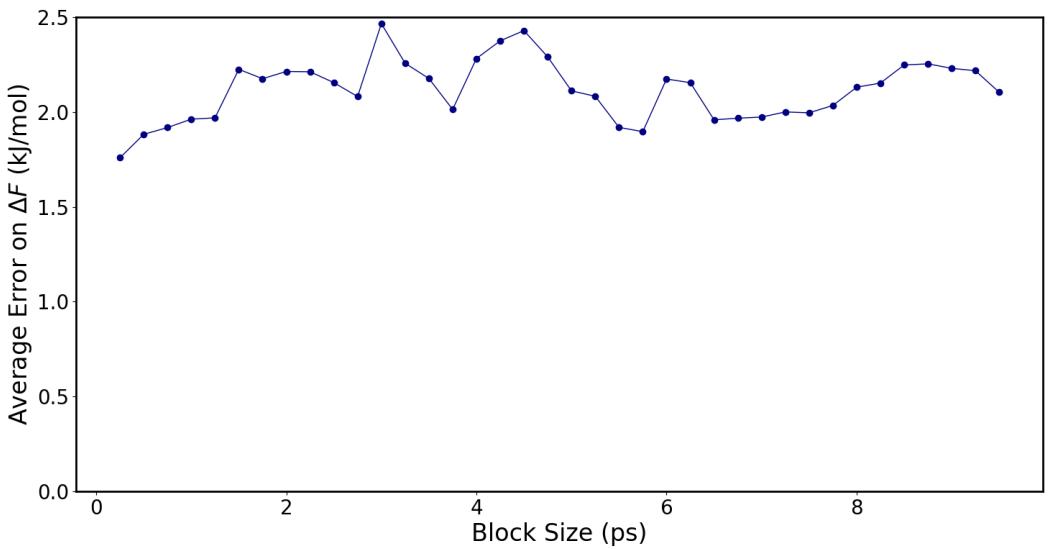
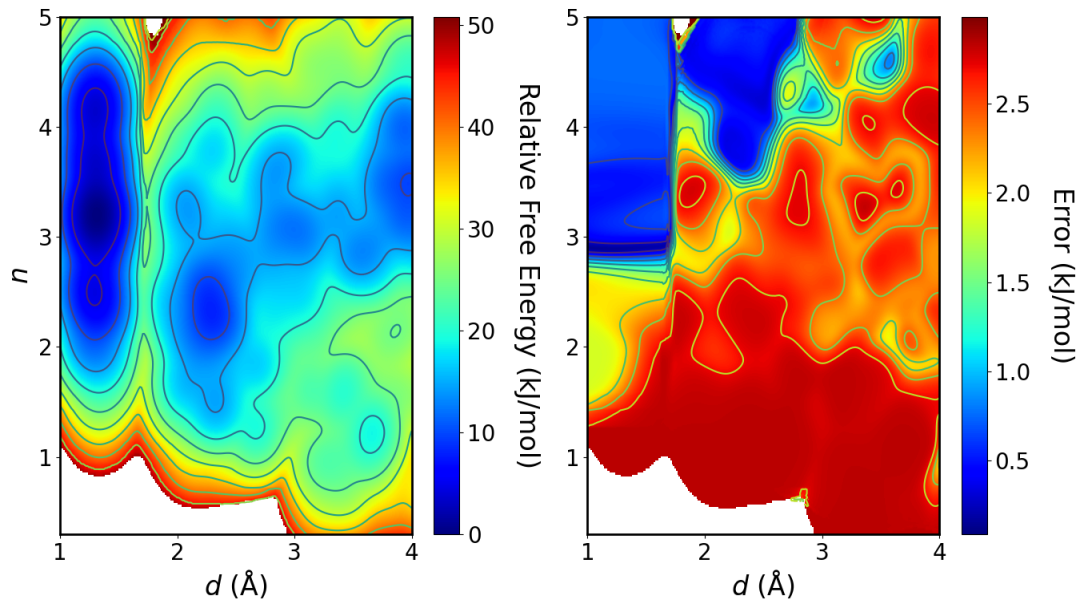


Figure S6: The deposition of Gaussians for the two walkers in the multiple walkers well-tempered metadynamics simulation.



(a) The average error of the free energy surface against block size.



(b) The free energy surface obtained with a block size of 9.5 ps (left) and the associated error (right).

Figure S7

S6: Computational Details on the Master Equation Model

We employed a master equation model to estimate the quantum yields of both channels after NO_3^- being excited to the T_1 state. The transition probability matrix (\mathbf{W}) of our master equation model consisted of the rate constants of the dissociation processes on the T_1 state free energy surface and the non-radiative deactivation processes:

$$\mathbf{W} = \begin{bmatrix} 0 & k_{A0} & k_{B0} & 0 & 0 \\ 0 & -(k_{A0} + 3k_{AB}) & 3k_{BA} & 0 & 0 \\ 0 & 3k_{AB} & -(k_{B0} + 3k_{BA} + 3k_{BC} + 3k_{BD}) & 0 & 0 \\ 0 & 0 & 3k_{BC} & 0 & 0 \\ 0 & 0 & 3k_{BD} & 0 & 0 \end{bmatrix}$$

Where the subscripts correspond to the transitions between two states. State 0 corresponds to $\text{NO}_3^- (\text{S}_0)$. States A, B, C, and D correspond to the 4 meta-stable states on the free energy surface in Figure 4. For example, k_{A0} corresponds to the intersystem crossing rate constant from $\text{NO}_3^- (\text{T}_1)$ to $\text{NO}_3^- (\text{S}_0)$. The initial population is fully occupied with state A ($\text{NO}_3^- (\text{T}_1)$) with a value of 0.043 under the assumption of NO_3^- absorbing photons at a wavelength of 313 nm. The population is propagated by \mathbf{W} , and the master equations are integrated by the fourth-order Runge-Kutta method. Here, we assume no recombinations will occur once state C or D is reached from state B.

Two kinds of rate constants are present in \mathbf{W} : the rate constants of transitions between the free energy minima and the intersystem crossing (ISC) rate constants. We apply the simple transition state theory[2] to estimate the rate constants on the free energy surface:

$$k_{TST} = \nu \exp\left(-\frac{\Delta F}{k_B T}\right)$$

Where ΔF is the free energy barrier of the transition, k_B is the Boltzmann constant, and T is the temperature. ν is the N-O1 vibrational frequency in states A and B, which is obtained by examining the vibrational density of states through the Fourier transform of the velocity autocorrelation function. The obtained N-O1 stretching frequencies in states A and B are 36 and 3.9 THz, respectively. These rate constants are multiplied with a factor of 3 to consider all three N-O bonds in NO_3^- .

To assess the non-radiative deactivation rates, we calculated the ISC rate constant from $\text{NO}_3^- (\text{T}_1)$ to $\text{NO}_3^- (\text{S}_0)$ and the ISC rate constant from the solvation cage complex (SCC) at the T_1 state to the S_0 state by the recently developed method using Fermi's golden rule combined with the path integral approach. [3, 4] This method includes the coupling of electronic spin-orbit coupling with vibrational degrees of freedom, which can describe the ISC rates of small organic molecules with negligible electronic spin-orbit coupling. [5]:

$$k_{ISC} = \frac{2\pi}{\hbar} \sum_{\nu, \nu'} P_{\text{T}_1, \nu}(T) |\langle \Phi_{\text{T}_1} \Theta_{\text{T}_1, \nu} | \hat{H}_{\text{SOC}} | \Phi_{\text{S}_0} \Theta_{\text{S}_0, \nu'} \rangle|^2 \delta(E_{\text{T}_1, \nu} - E_{\text{S}_0, \nu'})$$

Where Φ is the electronic and Θ is the vibrational wavefunction. $P_{\text{T}_1, \nu}(T)$ is the Boltzmann population of the vibrational state $\Theta_{\text{T}_1, \nu}$ in the T_1 state at a certain temperature T , and \hat{H}_{SOC} is the spin-orbit coupling operator. The coupling matrix element is expanded into a Taylor expansion in the normal coordinates Q around the final state (i.e., the S_0 state in this study) as the reference configuration ($Q = 0$):

$$\begin{aligned} \langle \Phi_{\text{T}_1} \Theta_{\text{T}_1, \nu} | \hat{H}_{\text{SOC}} | \Phi_{\text{S}_0} \Theta_{\text{S}_0, \nu'} \rangle = & (\langle \Phi_{\text{T}_1} | \hat{H}_{\text{SOC}} | \Phi_{\text{S}_0} \rangle)_0 \langle \Theta_{\text{T}_1, \nu} | \Theta_{\text{S}_0, \nu'} \rangle \\ & + \sum_k \left(\frac{\partial \langle \Phi_{\text{T}_1} | \hat{H}_{\text{SOC}} | \Phi_{\text{S}_0} \rangle}{\partial Q_k} \right)_0 \langle \Theta_{\text{T}_1, \nu} | Q_k | \Theta_{\text{S}_0, \nu'} \rangle \end{aligned}$$

The first term on the right-hand side is the electronic spin-orbit coupling matrix element, which is the so-called Franck-Condon (FC) approximation. The second term on the right-hand side is the vibronic spin-orbit interaction, which is similar to the so-called Herzberg-Teller (HT) effect on the electronic transition dipoles coupled with normal coordinates. A recent benchmark study showed that this method can qualitatively estimate the ISC rates of small organic aromatic molecules. [6]

All ISC rate calculations were performed at the level of TD-DFT with CAM-B3LYP functional and ma-def2-TZVP basis set using the ESD module in ORCA 5.0.4. The spin-orbit coupling operator was calculated by specifying the "SOCFlags = 1,4,3,0" option. The previous benchmark study showed that this is the lowest level of approximation to provide reliable results on ISC rates. [6] Other settings were set as default, and HT effect and Duschinsky rotations were included in the calculations. [7] Estimating the ISC rate using the method mentioned above requires one to calculate the Hessian matrices of the minima of the T₁ and the S₀ states. However, the Hessian matrices of the minima are not strictly available for structures under explicit solvation at a finite temperature, as the matrices contain imaginary frequencies. Performing geometry optimization on configurations with explicit solvation will cause the dynamic information of the solvated system to be lost. Under this circumstance, the Hessian matrices were obtained in three ways:

- 1 The Hessian matrices were obtained by the geometry optimizations followed by frequency calculations of the two structures in the gas phase.
- 2 The Hessian matrices were obtained by the geometry optimizations followed by frequency calculations of the two structures under the CPCM implicit solvation model.
- 3 The Hessian matrices were obtained from the frequency calculations of the free energy minima from the AIMD simulations. A hybrid solvation scheme was used with the first two solvation shells (12 water molecules) and the implicit CPCM solvation model. The imaginary frequencies were removed.

For the ISC rate from NO₃⁻(T₁) to NO₃⁻(S₀), the structure of NO₃⁻(T₁) was optimized at the level of TD-DFT with CAM-B3LYP functional and ma-def2-TZVP basis set, and the structure of NO₃⁻(S₀) was optimized at the level of DFT with the same functional and basis set for methods 1 and 2. Method 3 was not used to obtain the Hessian matrices in this case since the equilibrium configurations between NO₃⁻(T₁) and NO₃⁻(S₀) under explicit solvation are more displaced from each other, the harmonic approximation in this case may fail.

For the ISC rate from the SCC(T₁) to the SCC(S₀), the configuration of [NO₂ · · · O]⁻ without explicit solvation in state B on the free energy surface was optimized in the gas phase and under the CPCM implicit solvation model for methods 1 and 2, which leads to the minimum energy crossing point (MECP) between the T₁ and S₀ states. For method 3, the configuration in state B with the first two solvation shells on the free energy surface was directly used for both states. The frequency calculations in all these three methods were performed at the level of broken-symmetry DFT with CAM-B3LYP functional and ma-def2-TZVP basis set.

For both transitions, the ISC rate was calculated as the weighted average of the ISC rates from the three triplet spin sublevels, where the weight of each triplet sublevel was determined by its relative Boltzmann population at 300 K:

$$k_{ISC}^{av} = \frac{k_{ISC}^1 + k_{ISC}^2 e^{-\frac{\Delta E_{1,2}}{k_B T}} + k_{ISC}^3 e^{-\frac{\Delta E_{1,3}}{k_B T}}}{1 + e^{-\frac{\Delta E_{1,2}}{k_B T}} + e^{-\frac{\Delta E_{1,3}}{k_B T}}}$$

Where k_{ISC}^1 is the ISC rate constant from the first sublevel of T₁ state to S₀ state and $\Delta E_{1,2}$ is the energy difference between the first and second sublevels of T₁ state. The ISC rates for both transitions and their respective FC and HT contributions are summarized in Table S4. For the ISC rate from NO₃⁻(T₁) to NO₃⁻(S₀), it is about 50 times lower under the implicit solvation model than the gas-phase (Table S4). We note that the HT contribution for this ISC rate is 100%, which indicates that the ISC rate from NO₃⁻(T₁) to NO₃⁻(S₀) is entirely allowed by the vibronic spin-orbit coupling interaction. This also suggests that the quality of the Hessian matrices between the two states is crucial to obtaining a reliable estimate of the ISC rate. Therefore, this rationalizes not to apply method 3 to calculate the Hessians of the two states. Under these circumstances, the ISC rate calculated from method 2 was used for the master equation model to describe the ISC from NO₃⁻(T₁) to NO₃⁻(S₀).

For the ISC rate from the SCC(T₁) to the SCC(S₀), the three methods show the same order of magnitude (Table S4). We note that the HT contribution for this ISC rate has a maximum of ~10%, which indicates that the ISC rate from the SCC(T₁) to the SCC(S₀) is mainly contributed by the electronic spin-orbit coupling. Since the HT contribution is low in this case, the error contributed by the Hessian matrices in method 3 is acceptable. The reason for the ISC rate from the SCC(T₁) to the SCC(S₀) being much faster than the case of intact NO₃⁻ may be due to the nature of the SCC, which is an ensemble of MECPs between

Table S4: ISC rate constants for the two transitions calculated by the three methods and their respective FC and HT contributions. The ISC rate is the weighted average of the three triplet spin sublevels. The FC and HT contributions are the weighted average of the three spin sublevels.

Transitions	Method for Hessian	ISC rate constant (s^{-1})	FC (%)	HT (%)
$\text{NO}_3^-(\text{T}_1) \rightarrow \text{NO}_3^-(\text{S}_0)$	1	5.5×10^8	0.00	100.00
$\text{NO}_3^-(\text{T}_1) \rightarrow \text{NO}_3^-(\text{S}_0)$	2	1.2×10^7	0.00	100.00
$\text{SCC}(\text{T}_1) \rightarrow \text{SCC}(\text{S}_0)$	1	5.9×10^{12}	98.34	1.66
$\text{SCC}(\text{T}_1) \rightarrow \text{SCC}(\text{S}_0)$	2	5.5×10^{12}	96.56	3.44
$\text{SCC}(\text{T}_1) \rightarrow \text{SCC}(\text{S}_0)$	3	5.1×10^{12}	89.78	10.22

Table S5: The rate constants of the relevant transitions in NO_3^- photolysis. The uncertainties of the rate constants from the free energy barriers are obtained through the propagation of errors.

Transition	Average Rate Constant (s^{-1})
A→GS $\text{NO}_3^-(\text{T}_1) \rightarrow \text{NO}_3^-(\text{S}_0)$	1.2×10^7
A→B $\text{NO}_3^-(\text{T}_1) \rightarrow [\text{NO}_2 \cdots \text{O}]^-(\text{T}_1)$	$(1 \pm 1) \times 10^{10}$
B→A $[\text{NO}_2 \cdots \text{O}]^-(\text{T}_1) \rightarrow \text{NO}_3^-(\text{T}_1)$	$(7 \pm 6) \times 10^{10}$
B→GS $[\text{NO}_2 \cdots \text{O}]^-(\text{T}_1) \rightarrow [\text{NO}_2 \cdots \text{O}]^-(\text{S}_0)$	5.1×10^{12}
B→C $[\text{NO}_2 \cdots \text{O}]^-(\text{T}_1) \rightarrow \text{NO}_2 + \text{O}^\bullet$	$(2 \pm 2) \times 10^{10}$
B→D $[\text{NO}_2 \cdots \text{O}]^-(\text{T}_1) \rightarrow \text{NO}_2^- + \text{O} (^3\text{P})$	$(8 \pm 8) \times 10^{11}$

the T_1 and S_0 states. In fact, the ISC rate calculated without MECP optimization (method 3) is close to the one calculated with MECP optimization under the implicit solvation model (method 2). Therefore, the ISC rate calculated from method 3 was used for the master equation model to describe the ISC from the $\text{SCC}(\text{T}_1)$ to the $\text{SCC}(\text{S}_0)$.

References

- [1] Alex P. Gaiduk, Cui Zhang, François Gygi, and Giulia Galli, “Structural and electronic properties of aqueous NaCl solutions from ab initio molecular dynamics simulations with hybrid density functionals”, *Chem. Phys. Lett.* **604**, pp. 89–96 (2014).
- [2] Peter Hänggi, Peter Talkner, and Michal Borkovec, “Reaction-rate theory: fifty years after Kramers”, *Rev. Mod. Phys.* **62**(2), pp. 251–341 (1990).
- [3] Bernardo de Souza, Giliandro Farias, Frank Neese, and Róbert Izsák, “Predicting Phosphorescence Rates of Light Organic Molecules Using Time-Dependent Density Functional Theory and the Path Integral Approach to Dynamics”, *J. Chem. Theory Comput.* **15**(3), pp. 1896–1904 (2019).
- [4] Bernardo de Souza, Frank Neese, and Róbert Izsák, “On the theoretical prediction of fluorescence rates from first principles using the path integral approach”, *J. Chem. Phys.* **148**(3), pp. 034104 (2018).
- [5] Thomas J. Penfold, Etienne Gindensperger, Chantal Daniel, and Christel M. Marian, “Spin-Vibronic Mechanism for Intersystem Crossing”, *Chem. Rev.* **118**(15), pp. 6975–7025 (2018).
- [6] Koen Veys, Manon H. E. Bousquet, Denis Jacquemin, and Daniel Escudero, “Modeling the Fluorescence Quantum Yields of Aromatic Compounds: Benchmarking the Machinery to Compute Intersystem Crossing Rates”, *J. Chem. Theory Comput.* **19**(24), pp. 9344–9357 (2023).
- [7] Alberto Baiardi, Julien Bloino, and Vincenzo Barone, “General Time Dependent Approach to Vibronic Spectroscopy Including Franck–Condon, Herzberg–Teller, and Duschinsky Effects”, *J. Chem. Theory Comput.* **9**(9), pp. 4097–4115 (2013).